The Design and Analysis of a Rotman Lens with Reduced Conjugate-Port Coupling

by

Alex Ibbotson

Thesis presented in partial fulfilment of the requirements for the degree Master of Science in Engineering at Stellenbosch University

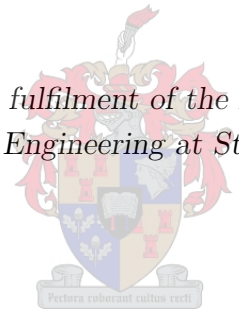

Supervisors:

Dr. D.I.L. de Villiers Prof. K.D. Palmer

December 2012

Declaration

By submitting this thesis electronically, I declare that the entirety of the work contained therein is my own, original work, that I am the sole author thereof (save to the extent explicitly otherwise stated), that reproduction and publication thereof by Stellenbosch University will not infringe any third party rights and that I have not previously in its entirety or in part submitted it for obtaining any qualification.

Date: November 2012 .....

Abstract

This project comprises the design, analysis, and construction of a Rotman lens with reduced conjugate-port coupling. The Rotman lens is a beam-forming network, used in wide-angle scanners to feed an antenna array. The scanning operation is based on optics and is therefore frequency invariant, a desirable feature of the Rotman lens compared to other beam-forming networks which employ phase shifters.

The antenna array is connected to the lens's array ports via transmission lines. These array ports lie on the array contour which is designed so that a signal incident onto the antenna array will propagate into the lens and focus at a particular point. The position of this focal point depends on the signals direction of arrival at the array. Ports are placed on these focal points to feed and receive signals. Bootlace lenses allow up to four focal points for linear arrays whereas the Rotman lens is designed for three foci. Scanners usually require to scan many beam-widths, thus ports are employed along a focal arc which intersect these foci. Inter-focal ports do not focus perfectly and result in phase errors distributed across the array aperture.

The derivation of three and four foci lenses is provided. There are several degrees of freedom at the designer's disposal, the effect which these available parameters have on the lens geometry and phase errors is investigated. The waveguide implementation of these lenses is examined, in which we use vertically polarised horns as feed ports and coaxial probes as array ports.

Some designs of Rotman lenses published in literature show excess mutual coupling between symmetrically opposed feed ports. Using a model which approximates the array contour as a reflecting wall, we show that this is due to the reflected energy focusing on conjugate ports. It is identified that Rotman lenses designed for minimum phase errors will have near maximum conjugate-port coupling.

Two Rotman lenses have been designed at $3,5$GHz for five feed ports, eleven elements, and up to $\pm 30^\circ$ scan angles. The first is designed for minimum phase errors, and the second for the defocusing of the reflected energy from the focal arc. Simulations show up to a 10dB reduction in conjugate-port coupling for the second lens with a negligible degradation in performance from the phase errors. Measurements show that the reflected energy is spread between the feed ports as expected, compared to the focusing at a single port of the traditional Rotman lens.

Uittreksel

Hierdie projek behels die ontwerp, analise en konstruksie van 'n Rotmanlens met verminderde simmetries oorstaande poort koppeling. Die Rotmanlens is 'n patroonvormingsnetwerk wat gebruik word as samestellingvoer in wye hoek skandeerders. 'n Gewensde eienskap van die Rotmanlens bo faseskuif voernetwerke is dat die skandeerwerking gebasseer is op optika en dus frekwensie onafhanklik is.

Die antennasamestelling word deur transmissielyne verbind aan die antennapoorte van die lens. Hierdie poorte lê op die samestellingkontoer wat ontwerp is om te verseker dat seine wat inval op die antennasamestelling sal voortplant in die lens en fokus op 'n spesifieke punt. Die posisie van die fokuspunt hang af van die invalshoek van die sein op die samestelling. Poorte word op hierdie fokuspunte geplaas om te seine te ontvang en te lanseer. Hierdie tipe lense kan tot vier fokuspunte hê , waar die Rotman lens spesifiek vir drie fokuspunte ontwerp word. Skandeerders moet normaalweg etlike bundelwydtes wyd kan skandeer, en daarom word poorte geplaas op 'n straal wat die fokuspunte onderskep. Poorte wat weg van die fokus geplaas word toon 'n effens uit fokus gedrag, wat vertaal na fasefoute in die samestelling stralingsvlak.

Die afleiding van drie en vier fokus lense word verskaf. Daar is verskeie grade van vryheid tot die beskikking van die ontwerper, en die effek wat die beskikbare parameters op die geometrie van die lens en die fase foute het word ondersoek. Die golfleier implimetering van hierdie lense word beskryf, waar vertikaal gepolariseerde horings as voerpoorte, en ko-aksiale lyne as antennapoorte gebruik word.

Sommige Rotman lens ontwerpe in die literatuur toon beduidende koppeling tussen die simmetries oorstaande voerpoorte. Deur van 'n model gebruik te maak wat die samestellingkontoer as 'n weerkaatsende muur benader toon ons aan dat die koppeling geskied as gevolg van die weerkaatsde energie wat fokus in die simmetries oorstaande poorte. Dit word identifiseer dat Rotman lense wat vir minimum fasefoute ontwerp word bykans maksimum koppeling tussen simmetries oorstaande poorte tot gevolg het.

Twee Rotman lense is ontwerp by $3,5$GHz vir vyf voerpoorte, elf antenna elemente en skandeer hoeke van ± 30. Die eerste is ontwerp vir minimum fasefoute en die tweede vir uit fokus weerkaatsde energie vanuit die fokus straal. Simulasies toon

tot 10 dB vermindering in koppeling tussen simmetries oorstaande poorte vir die tweede lens met weglaatbare werkverrigting verswakking as gevolg van fasefoute. Metings toon dat die weerkaatsde energie, soos verwag, versprei word tussen die voerpoorte vergeleke met energie gefokus in 'n enkele poort soos by die tradisionele Rotman lens.

Acknowledgements

I would like to express my sincere gratitude to the following people and organisations who have contributed to making this work possible:

- Dr. DIL de Villiers and Prof. KD Palmer of the University of Stellenbosch as my supervisors,
- The CSIR for funding the research,
- Mr Wessel Croukamp for assistance in the manufacturing and assembly of components,
- Mr Rob Anderson for assistance in the measurements.

Dedications

This thesis is dedicated to my wife,
Sheree Ibbotson,
for her support and love.

Contents

Chapter 1

Introduction

1.1 About the Project

This project comprises the design, analysis, and construction of a Rotman lens with reduced conjugate-port coupling. The Rotman lens is a popular beam-forming device, widely employed in the radar industry since its unveiling in the 1960's by W. Rotman and R.F. Turner[1]. It is functionally similar to that of a Butler matrix[2], but the Rotman lens was more robust and cost effective[1]. Moreover, it allowed for simultaneous and frequency invariant beam forming, a requirement for effective RADAR jamming[3]. The biggest remaining advantage of a Rotman lens over similar devices today, is its reduction in complexity for use in large wide-angle arrays[3][4][5].

A device which causes an incident electromagnetic wave to travel *through* it and come into focus at one or more points is known as a lens antenna[6][7]. The Rotman lens is of the Bootlace lens type, which is not an antenna itself but is rather implemented in wide-angle scanners to feed an antenna array. Its evolution from the lens antenna is discussed in the literature study. Whereas the Rotman lens is generally implemented in linear arrays for up to 90° scan angles, alternative Bootlace lenses are used for arc or circular arrays for up to 360° scan angles[3]. These lenses are utilised from millimeter frequencies to frequencies of a few meters, and are most commonly implemented in microstrip or waveguide form[4]. Whereas waveguide lenses provide better power handling, microstrip lenses achieve broader bandwidths[5].

The scanning operation functions similar to that of an optical lens, thus the analysis and design is based on ray-tracing techniques. The Rotman lens is made up of an electrically large parallel plate region with feed ports on the one side and array ports on the other side. The array ports are connected to the antenna array via trans-

mission lines which vary in length according to design. When a signal is generated at a feed port the energy radiates across the parallel plate region and couples into the array ports. Depending where the feed port is located in reference to the array ports, a phase gradient is created at the array aperture which steers the beam. The array ports lie on what is called the array contour, and the shape of this contour is designed so that all path-lengths traced from a source point to the phase front are equal. These source points are the lens's foci, and the Rotman lens uses three; one on-axis and two symmetrical about the axis. Bootlace lenses also allow for four foci, though quadrifocal lenses have one less degree of freedom at the cost of the extra focal point. In this project we compare trifocal and quadrifocal lenses and show that, except for a specific case, trifocal lenses perform better.

Scanning arrays usually require many beams, thus the lens also makes use of feed ports positioned between the foci, on a focal arc. An array fed from non-focal sources on the focal arc do not hold equal path-lengths to the required phase front, and thus have an associated phase error. Three and four foci lenses have a phase error that is cubic in its distribution across the array aperture, causing a tilt in the beam direction and a reduction in directivity[6]. Traditionally, Rotman lenses refocus the focal arc for near minimum phase errors using an equation derived by J. Ruze[8][9].

The open spaces between the edge feed port and the edge array port are called the lens sidewalls. Together, the beam ports, array ports, and sidewalls form a closed electrically-large parallel plate structure that suffers from multiple reflection paths, since ports do not fully absorb all the energy incident on them. Energy radiated from a port will essentially reflect throughout the parallel plate region several times before dissipating. This causes unwanted coupling between certain ports, and is historically the biggest contributor as to why some of these lenses fail industry standards[10]. Typically, absorbing material or matched dummy ports are used along the sidewalls to reduce reflections. Larger sidewalls allow for a signal to be absorbed multiple times before radiating back into the lens, but greatly increases the structure size.

In some designs published in the literature, it is seen that feed ports symmetrically opposed from each other have their mutual coupling level up to and over 10dB higher than for the other ports[2][11]. It is known that reflections off the array contour are responsible for the excess coupling[2], although this is not widely investigated. Using a simplified model which approximates the array ports as a reflecting wall, excess conjugate-port coupling can be predicted by tracing reflections off the

array contour. The model ignores coupling and reflection coefficients at the ports and therefore cannot predict the exact level of coupling, it does however show where the reflections focus. Simulations of a few different lenses agree, the closer the reflections' focus is to the port the larger the degree of coupling.

The trifocal lens parameters allow for design freedom. In this thesis the effect of various array contour curvatures on the level of conjugate-port coupling is investigated. A trade off between the phase error distribution and the conjugate-port coupling is identified, and it is shown that using a traditional Rotman lens provides for near maximum conjugate-port coupling. This coupling may be reduced by using an array contour which produces non-minimal phase errors. It is shown that, for most practical lenses, the increase in phase errors results in only a negligible reduction in radiation performance with a marked improvement in conjugate-port coupling.

In this project a Rotman lens is designed and fabricated in waveguide for 5 feed ports, 11 array elements, a centre frequency of 3.5GHz, $\pm 30^\circ$ scan angles, and reduced conjugate-port coupling. Simulations of the lens shows conjugate-port coupling of up to 10dB less than that of a traditional Rotman lens, whereas the measurements show couplings which are further reduced. The lens achieves 13% bandwidth at the -10dB level, where the side-lobe levels of the radiation pattern is about -13dB. Building the traditional Rotman lens in waveguide is a future project which will allow for better comparison between the lenses.

1.2 About the Report

The Rotman lens is a type of Bootlace lens, which is designed for three focal points. In chapter two we discuss the origin of these lenses and the popular variations used. In chapter three we derive the lens equations for Rotman as well quadrifocal lenses, for comparison. The lens geometry affects the performance of these lenses, thus we also analyse the effect the parameters have on the geometry and corresponding phase aberrations. We conclude the chapter with a general design procedure for these lenses.

In chapter four we detail the implementation of these lenses in waveguide form for vertical electric-field polarisation, and again provide a design procedure. In chapter five we simulate a traditional Rotman lens, analyse its performance regarding conjugate-port coupling, and apply approximation models to predict the severity of this coupling. In chapter six we design, simulate and measure a Rotman lens for the

same specifications, but with the reflections defocused from the feed ports. Finally, we conclude in chapter 7.

Chapter 2

Literature Study

2.1 Introduction

The Rotman lens is of the Bootlace lens type, a constrained optical scanner. In this chapter we study the origins of the Bootlace lens and provide a brief history of its evolution from the lens antenna. We investigate the function of the lens and how it is implemented. The two most popular Bootlace lenses are then discussed.

2.2 The Bootlace Lens Origins

2.2.1 Normal Metal Lens Antennas

When someone reads the word lens they will often imagine an optical lens, such as a magnifying glass or a camera lens. These lenses are used to bring light into focus by means of refraction. The field of antennas has adopted the same technique. A device which causes an incident electromagnetic (EM) wave to travel *through* it and come into focus at one or more points is known as a lens antenna. This should not be confused with reflector antennas where the focusing is due to the reflections off a shaped dish.

Lens antennas are classified according to the material from which they are constructed[6]. Figure 2.1 depicts the dielectric lens antenna which requires a convex shape, the same as what is used in optics. Compare this to figure 2.2 which shows a metal-lens antenna, concave in shape. Both classes achieve the same outcome but use different geometries according to how the EM rays refract through the lens.

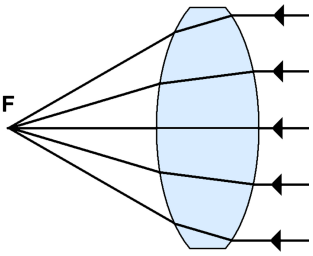

Figure 2.1: A dielectric lens, with a refractive index > 1.

Lens design is accomplished by using the optical ray theorem[12] which states that the optical path-lengths between two constant phase fronts are equal. Simply put, multiple in-phase EM rays which travel the exact same distance will still be in phase. We call the distances that these rays travel their path-lengths. Analysis of EM waves by tracing their path-lengths is commonly known as the ray-tracing technique. Beam forming is therefore achieved by designing a lens for equal path-lengths between a point source and the desired EM wave front. These lens antennas are "true-time delay" devices in that their beam forming operation is entirely mechanical. This tells us that they are inherently frequency independent. However, limitations on the achievable frequency bandwidth come from and depend on the components used to fabricate the lens antenna, such as the feed port.

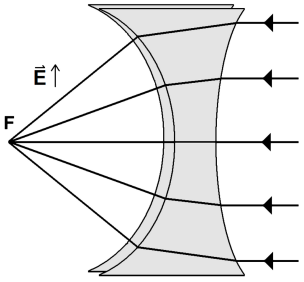

Figure 2.2: A metal-lens antenna, using stacked metal plates to achieve a refractive index < 1.

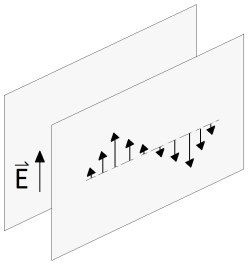

Figure 2.3: Two parallel plates of the normal metal lens of figure 2.2 showing the direction of the electric field vector.

W. E. Kock described some of the first metal-lens antennas[13] in 1946. They consist of waveguides made by thin parallel conducting plates. Their operation is based on the fact that a non-TEM wave confined in a waveguide has a phase velocity

greater than its free space phase velocity. This phase velocity of a TE_1 mode wave is given by

$$v = v_0/\sqrt{1-(\lambda/2a)^2} \tag{2.1}$$

where v_0 is the free space velocity, λ is the free space wavelength, and a is the parallel plate seperation. The index of refraction of a medium is the ratio of the free space velocity to velocity in the medium (here the medium is the parallel plate region) which is then

$$\eta = \sqrt{1-(\lambda/2a)^2} \tag{2.2}$$

This represents an index of refraction smaller than one, in contrast to optical lenses which use dielectric materials with an index of refraction greater than one. Metal lens antennas therefore use a concave shaped lens for its focusing.

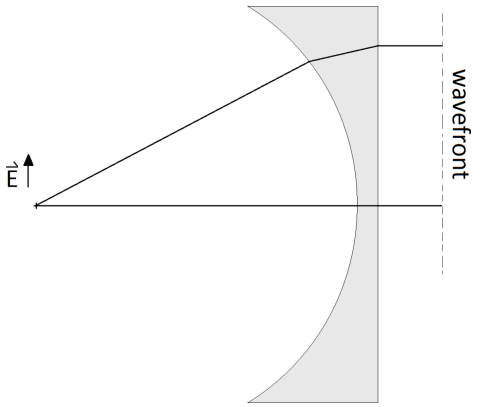

Figure 2.4: The side view of a normal metal lens antenna showing two different paths of an EM ray. The lens focal point F and the direction of the electric field vector $\vec{E}$ are shown.

Figure 2.4 shows a normal metal lens with focal point F and the direction of the electric field vector $\vec{E}$. Two paths of an EM ray are traced from the focal point to the transmitted, or received, linear EM wavefront. These two path-lengths are electrically equal. Figure 2.3 shows the configuration of the parallel plates of figure 2.4. The operation of normal lenses follows Snell's law of refraction. A waveguide horn is positioned on the focal point to transmit and receive signals. The resulting directivity and side-lobe levels of the antenna is mostly determined by the feed horn[13].

2.2.2 Constrained Metal Lens Antennas

The Bootlace lens is a type of metal-lens antenna. However, as J. Ruze shows, there exists two types of metal-lenses[9]. The first type is that of a "normal" metal-lens as previously shown in figure 2.4, where the second type is known as a constrained metal-lens. Although they are both classified as a metal-lens antenna, constrained metal-lenses do not obey Snell's law of refraction[9]. The EM wave is guided by the metal plates and their direction is not affected by the refractive index. Figure 2.5 illustrates a constrained metal-lens antenna. The three path-lengths drawn from the source to the EM wavefront are of equal electrical length. Like the normal metal-lens the TE_1 wave still has its electric field vector parallel to the conducting plates, but is now constrained by them.

Equation 2.1 still determines the phase velocity between the plates. Since the physical path lengths of the EM rays on the edges of the lens are longer than of those in the centre, the lens has to reduce the electrical length of paths further from the centre accordingly. Therefore the lens is either required to have longer waveguides at the edges as shown in figure 2.5 or the seperation of the waveguide side walls must decrease in width in order to increase the phase velocity according to equation 2.1. It is therefore also possible to design a constrained metal-lens without any curvature if the appropriate metal plate separation is applied[12].

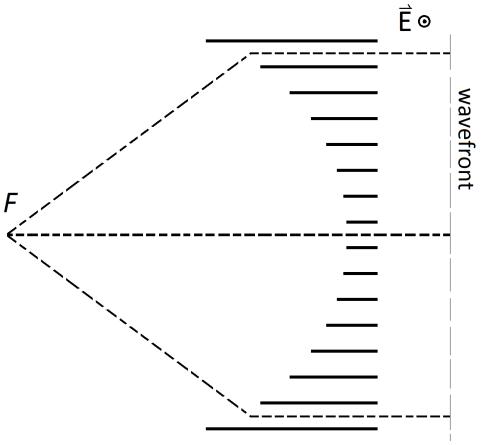

Figure 2.5: The top view of a constrained metal lens antenna of equal plate spacing. Three EM ray path lengths are shown from the focal point to the EM wavefront.

Normal metal-lens antennas are limited to a single focal point. In 1950, J.Ruze presented a constrained metal-lens antenna with two symmetrically positioned foci[9].

Thus the constrained metal-lens can be used as a multiple beam-forming device. For radar application the lens would be required to scan narrow beams over a wide angular region, only scanning the two angles on which the foci are positioned is not enough. J.Ruze therefore incorporated a focal arc which intersects the focal points. Scanning could then be achieved by moving a feed horn along the focal arc, or by placing fixed feed horns on it instead. Multiple beam-forming lenses are known as optical scanners[7].

Figure 2.6 shows a constrained metal-lens cross section used for wide-angle scanning. The three EM rays traced from one of the foci to the radiated EM wavefront show the operation of the lens. The inner scan angle α of the foci also result in a beam scan angle of α by design.

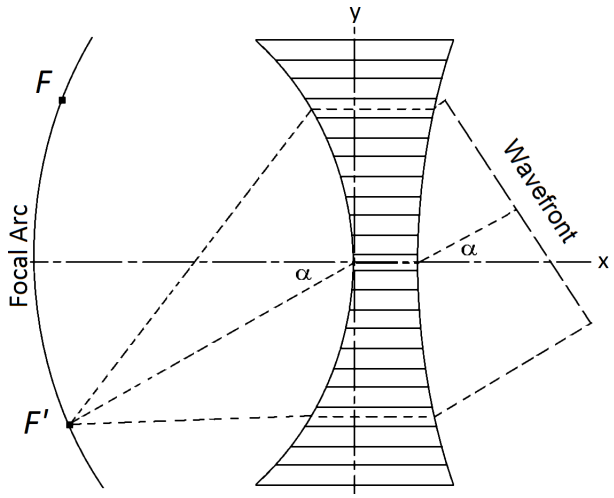

Figure 2.6: The cross section of a constrained metal-lens with two foci which radiate or receive a beam at a scan angle α.

The lens only achieves perfect focus at the two conjugate foci, EM rays emitted anywhere else on the focal arc will not all collimate at the wavefront in phase. This phase deviation causes distortion of the radiation, and is known as the phase error. The phase error of a lens largely determines its performance. J. Ruze expressed the phase error as a power series across the lens aperture as

$$\delta = ay + by^2 + cy^3 + dy^4 + ... \tag{2.3}$$

where the constants are functions of the lens parameters[9]. He also provided results for the refocusing of the focal arc for various constrained lens configurations, which minimises the phase errors. The linear phase error constant a introduces a tilt in

the beam, the quadratic phase error constant b causes a reduction in directivity, and the cubic phase error constant c results in both a tilt and a loss of directivity in the beam[6]. The refocusing of the focal arc can reduce or elliminate some of these errors.

2.2.3 The Bootlace Lens

In 1957, H. Gent presented an extra degree of freedom to the constrained lens of Ruze[8]. Gent's lens did not require the waveguide plates to meet the antenna aperture at the same height. For this reason, these parallel conducting plates are replaced by flexible transmission line, such as coaxial cable. Gent's lens has been named the Bootlace lens, because the flexible transmission line which connects the lens and the radiating array look similar to the laces on a boot. This new way of connecting a lens device has been greatly advantageous, as the array elements size and spacing are no longer confined to the parallel plate waveguides of the lens. Where the lens and the radiating aperture were the same part, they are now split into two different components, namely the lens and the antenna array. For this reason, the bootlace lens is not a metal-lens antenna although it is has been adapted from it. The only design parameters linking the lens and the antenna array are the number of elements on the array and the distance between these elements. Essentially, they are designed seperately.

In the 1960's there was a large demand for the bootlace lens due to its true-time delay capability[14] as it allows for simultaneous beam forming. It was also cheaper and more robust over its counter part - the butler matrix[1]. However, as technology progresses the main advantage of the Bootlace lens that seems to remain is its simplicity[3][10]. Popular Bootlace lens configurations are briefly discussed in the next section.

2.3 Popular Bootlace Lens Types and Implementations

2.3.1 The Rotman Lens

The Rotman lens is the most popularly implemented Bootlace lens device. In 1962, W. Rotman and R.F. Turner shared design equations for the trifocal bootlace lens[8]. Their lens applies refocusing of the focal arc as derived by Ruze[9]. This gives a "near optimum" design for a least phase error distribution[8]. Trifocal lenses have generally come to be labelled as Rotman lenses, whether they use the refocusing equation for the focal arc or not.

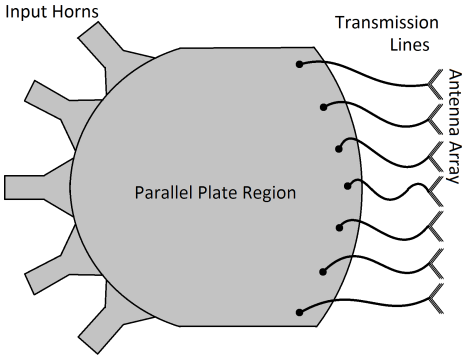

Figure 2.7: The top view of a Rotman lens implemented in waveguide.

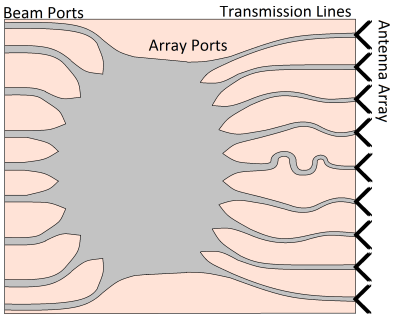

Figure 2.8: The top view of a Rotman lens printed on microstrip.

In figure 2.7 a standard implementation of a Rotman lens is shown in waveguide. Input horns lie on a circular focal arc. EM energy radiates within the parallel plate region, and coaxial probes are situated along the lens contour. Each probe is connected to antenna element on the antenna array via a transmission line. The five input horns represent five angles at which the device can transmit or receive a signal. Alternatively, a single input horn can be mechanically guided along the focal arc to provide finer beam steering. Lenses implemented in waveguide usually use a coaxial to waveguide transition which limits the attainable bandwidth to about twelve percent[5]. Techniques are available to improve this, such as tuning pins.

Due to cost, weight and bandwidth specifications, it is more common to find Rotman lenses implemented in microstrip or stripline. Figure 2.8 depicts how a typical microstrip Rotman lens would look like. Both beam ports and array ports are flared to provide a better impedance match between the port and the open propagation region. The required transmission line lengths are usually also printed on the microstrip board, which is then connected to the antenna array. Microstrip and stripline lenses employ materials with a relative dielectric constant ϵ_r. This reduces all the dimensions of the lens by a factor equal to $\sqrt{\epsilon_r}$. Waveguide lenses are usually air filled[15] and are therefore not as lossy, and allow for better power handeling. However, amplifiers and phase shifters can be built into the transmission line before the antenna array which can provide power amplification and fine steering[3].

Figure 2.9 shows a configuration on how to stack multiple Rotman lenses in order to provide scanning in two dimensions. This also gives a pencil beam shape as opposed to the conical fan beams of the linear array. Rotman lenses with curved array apertures can be stacked to fit conformal installations, such as on an aircraft[1].

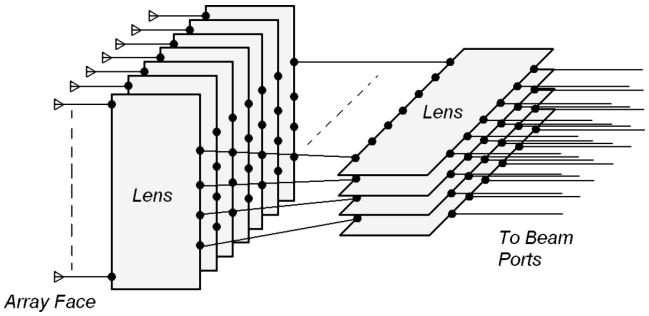

Figure 2.9: Rotman lens stacking to provide planar scanning.

2.3.2 R-2R and R-KR Lenses

Whereas the Rotman lens provides beam steering for straight-line and curved arrays, the R-2R and R-KR Bootlace lenses are used for circular arrays[1]. These lenses have their geometry made out of two concentric circles, one on which the feed and array ports lie with radius R, and the other on which the array elements lie with the radius a multiple of R. These are shown in figures 2.10 and 2.11. The R-2R has the array lie on a circle twice the size of the inner, and the R-KR has the array lie on a circle at K times the inner circle, K is usually used as 1.9. The figures illustrate the array ports and their positioning in relation to the angle it makes with the circle's centre.

The R-2R lens has the remarkable property of the entire focal arc being perfectly in focus, and it is the only bootlace lens with such a property[14]. Due to its array port placement, however, it is limited to a maximum 45° scan angle. The R-KR on the other hand does not have perfect focusing on the focal arc. Unlike the R-2R it uses equal-length transmission lines connected perpindicularly between the circles. Any feed port on the focal arc makes a beam which is steered in a direction directly opposite it. By using a circulator in the transmission lines, all the ports on the inner can be used as both the feed and array ports, and the R-KR lens can be can provide full 360° coverage.

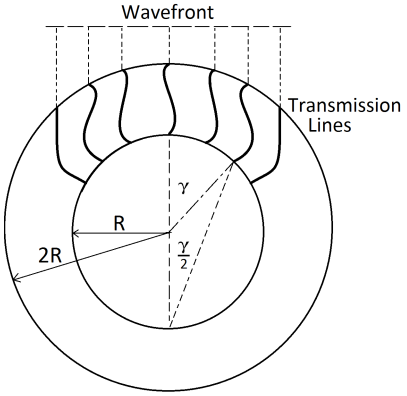

Figure 2.10: The geometry and operation of an R-2R Lens for perfect focusing along the focal arc.

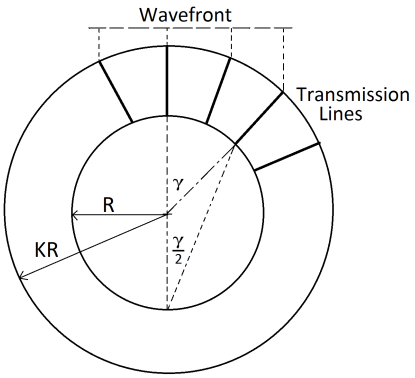

Figure 2.11: The geometry and operation of an R-KR Lens which can be rotated for full symmetry.

2.4 Conclusion

The origin of the Rotman lens has been described starting with the lens antenna. Its evolution takes it from a monofocal lens which uses refraction to a trifocal lens which is constrained. As an optical scanner, these lenses are analysed using path-lengths from a source to the required phase-front. Geometry is key in the designing and analysis of these lenses. Not all feed ports placed on the focal arc are perfectly in focus, and should therefore be designed for least aberrations. In the following chapter we derive the lens equations and analyse the geometry and associated phase errors.

Chapter 3

The Design of 3 and 4 foci lenses

3.1 Introduction

This chapter looks at the design of trifocal and quadrifocal lenses. With ray tracing, the lens design is entirely a geometrical problem. A derivation of the lens equations is provided for all ports, which shows that these lenses have several degrees of design freedom. A thorough analysis of the effect of these available parameters on both the lens geometry and phase errors is given. Using this approach, trifocal and quadrifocal lenses are compared.

The objective of this chapter is to be equipped with a thorough understanding of lens principles and design. We conclude with a general design procedure for these lenses. Implementing the lens into a manufacturable form is explored in the following chapter.

3.2 The Lens Design Equations

Our consideration of trifocal and quadrifocal lenses is convenient in that we can derive the trifocal lens as a special case of the quadrifocal lens. Where the quadrifocal lens uses two symmetrically conjugate foci, the trifocal lens uses one symmetrically conjugate foci and one on-axis focus. If the inner foci of the quadrifocal lens meet at the axis we have a trifocal lens. Here we derive the lens equations for linear array apertures. This derivation follows the same technique given by Rotman and Turner[8], and uses the coordinate system shown by Hansen[16], except we include an additional focal point. Although not followed, literature on quadrifocal lenses is widely available[15].

Figure 3.1 shows a diagram of a quadrifocal Bootlace lens. The lens consists of a parallel plate region connected to an antenna array via transmission lines,

symmetrical about the x-axis. On the one side of the parallel plate region is the beam contour with foci F_1 and F_2, and their conjugates, as in symmetry pairs, F_1' and F_2'. The foci points are the only points on the beam contour that are perfectly in focus, the rest of the beam contour is designed for least phase error. Generally an ellipse is used. Any point, P, on the array contour has coordinates (X,Y) and is connected by a transmission line of electrical length W to an antenna element on the antenna array with height N. The array contour intercepts the origin.

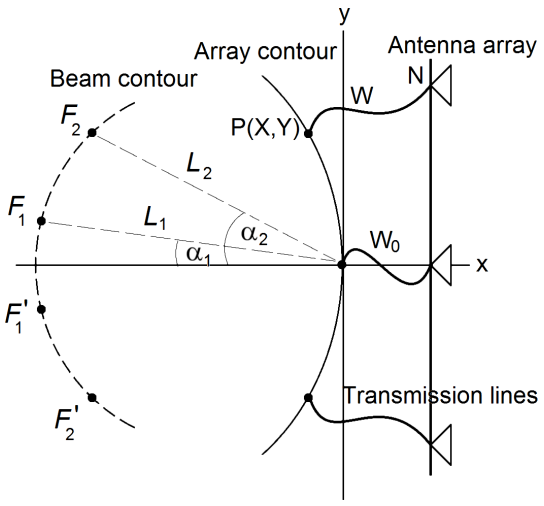

Figure 3.1: Geometry of a quadrifocal Bootlace lens.

Figure 3.2 shows the scanning operation of the lens. The array contour and the transmission line lengths are designed so that a focus point at an angle α will form a beam at a corresponding angle ψ. An on-axis beam port will form a broadside beam.

The lens variables are all normalised to focal length L_1. This determines the scale of the lens, and is usually expressed in wavelengths. The normalised parameters are expressed by their lower case counter parts, and the electrical length of the transmission lines are taken in reference to W_0, the on-axis electrical length.

$$x = X/L_1 \qquad y = Y/L_1 \qquad w = (W - W_0)/f_1$$
$$n = N/L_1 \qquad f_1 = F_1/L_1 \qquad f_2 = F_2/L_1$$

An important parameter is the focal ratio β, where

$$\beta = \frac{L_2}{L_1} \tag{3.1}$$

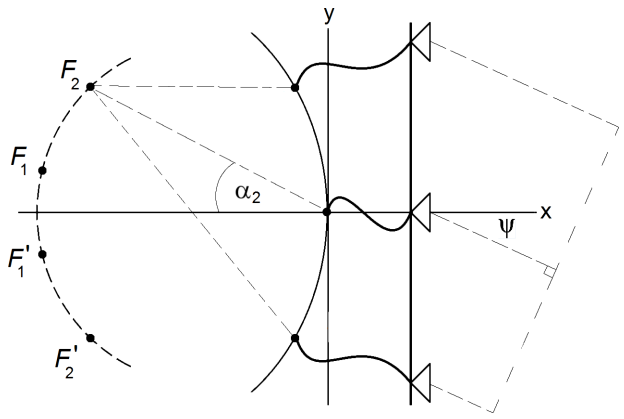

Figure 3.2: The beam forming operation of the lens.

The beam angle ψ, as in figure 3.2, is related to the edge focal angle by the angle ratio:

$$\gamma = \frac{\sin\psi}{\sin\alpha_2} \tag{3.2}$$

For amplitude and phase errors, Hansen[16] defined a parameter, ζ, to relate the height N of any point on the array to the focal length L_1:

$$\zeta = \frac{N\gamma}{L_1} = n\gamma \tag{3.3}$$

N is dependent on both the element number and the element spacing, d_e. Figure 3.3 labels the path lengths used to derive the lens equations.

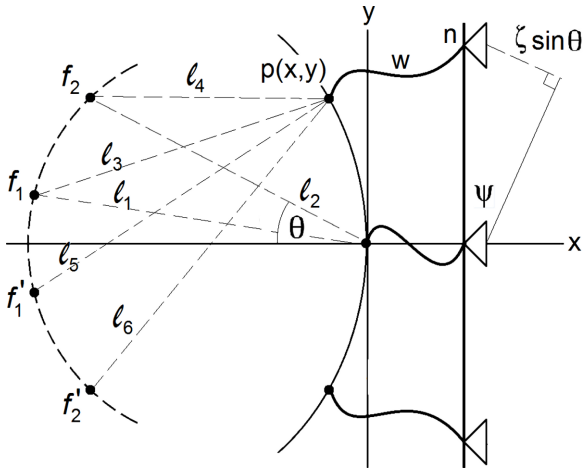

Figure 3.3: Diagram used for the lens equations.

For convenience let

$$\begin{aligned} C_1 &= \cos\alpha_1 & S_1 &= \sin\alpha_1 \\ C_2 &= \cos\alpha_2 & S_2 &= \sin\alpha_2 \end{aligned} \tag{3.4}$$

The normalised focal lengths are

$$l_1 = 1 \qquad l_2 = \beta \tag{3.5}$$

Therefore the foci coordinates are given by

$$f_1(x,y) = (-C_1, S_1) \qquad f_2(x,y) = (-\beta C_2, \beta S_2) \tag{3.6}$$

The required pathlength of a ray radiated from an antenna element to the desired wavefront is $n\sin\psi$. Note that any inner angle θ that a beam port makes with the origin is related to its corresponding beam angle ψ by the independent variable γ. Then, from equation 3.2, we can rewrite this to

$$n\sin\psi = \zeta\sin\theta \tag{3.7}$$

Note that α_2 is the edge focal angle and α_1 the inner focal angle. The focusing effect of the lens requires that the rays from a transmitting beam port collimate at the desired wavefront with equal path lengths, and vice versa for a receiving beam port. Therefore, for the focal point f_2 we have

$$l_2 = l_4 + w + \zeta S_2 \tag{3.8}$$

The magnitude of l_4 is given by

$$\begin{aligned} l_4^2 &= (-\beta C_2 - x)^2 + (\beta S_2 - y)^2 \\ &= \beta^2 + x^2 + y^2 + 2x\beta C_2 - 2y\beta S_2 \end{aligned} \tag{3.9}$$

From equation 3.5 and 3.8 we have

$$l_4 = \beta - w - \zeta S_2 \tag{3.10}$$

Then, substituting 3.10 into 3.9 we get

$$-2\beta w - 2\beta\zeta S_2 + w^2 + 2w\zeta S_2 + \zeta^2 S_2^2 = x^2 + y^2 + 2x\beta C_2 - 2y\beta S_2 \tag{3.11}$$

From the conjugate of focal point f_2 we have the equal path length

$$l_2 = l_6 + w - \zeta S_2 \tag{3.12}$$

The magnitude of l_6 is

$$\begin{aligned} l_6^2 &= (-\beta C_2 - x)^2 + (-\beta S_2 - y)^2 \\ &= \beta^2 + x^2 + y^2 + 2x\beta C_2 + 2y\beta S_2 \end{aligned} \tag{3.13}$$

From equation 3.5 and 3.12 we have

$$l_6 = \beta - w + \zeta S_2 \tag{3.14}$$

Substituting 3.14 into 3.13 we get

$$-2\beta w + 2\beta\zeta S_2 + w^2 - 2w\zeta S_2 + \zeta^2 S_2^2 = x^2 + y^2 + 2x\beta C_2 + 2y\beta S_2 \tag{3.15}$$

Now, comparing equations 3.11 and 3.15 we find that

$$\begin{aligned} &2\beta\zeta S_2 - 2w\zeta S_2 = 2y\beta S_2 \\ &\text{or } y = \zeta(1 - \frac{w}{\beta}) \end{aligned} \tag{3.16}$$

This process can be repeated for focal point f_1, or we simply substitute the angle and magnitude. Substituting $\beta = 1$ and $S_2 = S_1$ into equation 3.16 gives us

$$\begin{aligned} &2\zeta S_1 - 2w\zeta S_1 = 2yS_1 \\ &\text{or } y = \zeta(1 - w) \end{aligned} \tag{3.17}$$

Equations 3.16 and 3.17 cannot both be true, unless $\beta = 1$. The focal ratio is therefore limited to unity for quadrifocal lenses. However, this is not the case for trifocal lenses. By selecting a focal angle of zero, for foci f_1, the lens reduces to 3 focal points. We thus have $C_1 = 1$ and $S_1 = 0$. Equation 3.17 is no longer valid and we have freedom to choose the focal ratio, β. We will continue to solve for the lens parameters with the definition of a 4 foci lens as

$$\alpha_1 \neq 0 \qquad\qquad \beta = 1 \tag{3.18}$$

And the definition of a 3 foci lens as

$$\alpha_1 = 0 \tag{3.19}$$

Now, substituting equation 3.16 into 3.11 gives us

$$w^2 - 2\beta w + \zeta^2 S_2^2 = x^2 + y^2 + 2x\beta C_2 \tag{3.20}$$

Using the angle and magnitude of focal point f_1, the equivalent equation is

$$w^2 - 2w + \zeta^2 S_1^2 = x^2 + y^2 + 2xC_1 \tag{3.21}$$

Comparing these two equations gives us

$$-2w + 2\beta w + \zeta^2 S_1^2 - \zeta^2 S_2^2 = 2xC_1 - 2x\beta C_2 \tag{3.22}$$

which provides the solution for x as

$$x = \frac{2w(\beta - 1) + \zeta^2(S_1^2 - S_2^2)}{2(C_1 - \beta C_2)} \tag{3.23}$$

This shows that x is independant of w for quadrifocal lenses.

Now, substituting the solution of x (equation 3.23) and y (equation 3.16) into equation 3.21 gives us the solution of w as the quadratic function

$$\begin{aligned} & w^2 \left(\frac{(\beta - 1)^2}{(C_1 - \beta C_2)^2} + \frac{\zeta^2}{\beta^2} - 1 \right) \\ & + w \left(\frac{\zeta^2(\beta - 1)(S_1^2 - S_2^2)}{(C_1 - \beta C_2)^2} - \frac{2\zeta^2}{\beta} + \frac{2C_1(\beta - 1)}{C_1 - \beta C_2} + 2 \right) \\ & + \left(\frac{\zeta^4(S_1^2 - S_2^2)^2}{4(C_1 - \beta C_2)^2} + \zeta^2 + \frac{\zeta^2 C_1(S_1^2 - S_2^2)}{C_1 - \beta C_2} - \zeta^2 S_1^2 \right) \end{aligned} \tag{3.24}$$

With ζ given by the position of the antenna elements on the array from equation 3.3, we can solve for the array contour, parameters x and y, and the transmission line lengths, parameter w. Setting $\alpha_2 = 0$ for trifocal lenses, equation 3.24 agrees to that given in Hansen[16]. Next we define the focal arc of the lens.

Lenses which employ 5 foci require a conformal array compared to the linear array designed here.

3.3 The Lens Focal Arc

3.3.1 Introduction

The focal arc of the lens is known as the beam contour, for it is on this contour that the feed ports, also known as the beam ports, are placed. Only the foci allow for error-free beams, however, as we generally desire more than 3 or 4 beams, we position

the ports on a contour which intersects the foci. Generally an elliptical contour is used. Here we derive the parameters of this contour and the errors associated with it.

3.3.2 Elliptical beam contour

The Rotman lens typically uses a circular beam contour[8]. However, it has been shown that it may be advantageous to deviate slighty from a circular arc[16], so an elliptical contour is considered. Another approach uses beam and array contours which are symmetrical to each other[17], but is restricted in design freedom[7].

Here we derive the equations for an elliptical beam contour, and introduce the parameter ρ which sets the degree of ellipticity.

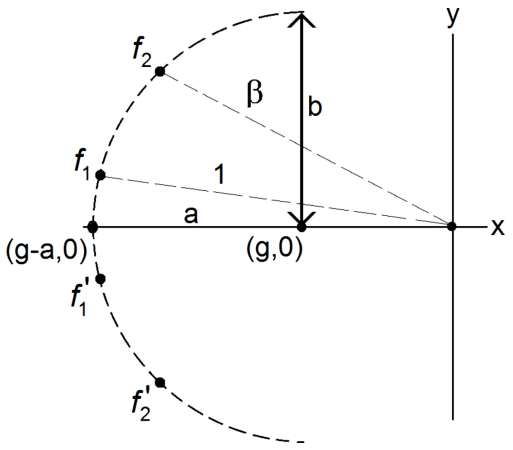

Figure 3.4: Elliptical focal arc.

Figure 3.4 shows the beam contour defined by an ellipse with width a, height b, and centre point $(g, 0)$. We will define the ellipticity, ρ, of the ellipse by the ratio

$$\rho = \frac{b}{a} \tag{3.25}$$

With respect to figure 3.4, the equation of the ellipse is given by

$$(\frac{x-g}{a})^2 + (\frac{y}{b})^2 = 1 \tag{3.26}$$

Focal points f_1 and f_2 have coordinates $(-C_1, S_1)$ and $(-\beta C_2, \beta S_2)$ respectively.

The centre point of the ellipse is then

$$g = \frac{\rho^2(C_1^2 - \beta^2 C_2^2) + (S_1^2 - \beta^2 S_2^2)}{2\rho^2(\beta C_2 - C_1)} \tag{3.27}$$

And the ellipse width is

$$a = \sqrt{(C_1 + g)^2 + S_1^2/\rho^2} \tag{3.28}$$

Then, any point on the ellipse with coordinates $(-h\cos\theta, h\sin\theta)$, as shown in figure 3.7, has the solution

$$h^2(\rho^2\cos^2\theta + \sin^2\theta) + h(2\rho^2 g\cos\theta) + \rho^2(g^2 - a^2) = 0 \tag{3.29}$$

Here we define θ has the lens angle. Any lens angle θ is related to its corresponding beam angle ψ by

$$\sin\psi = \gamma\sin\theta \tag{3.30}$$

as from equation 3.2.

Evenly spaced beams are usually required, thus the beam ports are placed on the beam contour such that their lens angles are evenly spaced. The edge beam port has a lens angle θ_{max} which corresponds to the maximum beam angle, ψ_{max}. Thus, a lens has a total scan sector of $2\psi_{max}$.

Now that all geometrical components of the 3 and 4 foci bootlace lenses have been established, figures 3.5 and 3.6 compare the normalised plots of a trifocal and quadrifocal lens which uses 7 beams and 9 array elements. For the trifocal lens the parameters are set to $\alpha_2 = 30°$, $\beta = 0.9$, $\psi_{max} = 40°$, $d_e = 0.5\lambda$, $L_1 = 4\lambda$, $\gamma = 1.1$, and $\rho = 1$. The quadrifocal lens differs in that β is restricted to unity, and here $\alpha_1 = 10°$.
The beam contour is shown on the left, and the array contour on the right. The port positions and foci of both contours have been marked. The β restriction of the quadrifocal lens forces a stronger curvature of the array contour. Next we derive the phase errors associated with these lenses.

3.3.3 Phase error

An optical abberation exists when light rays do not focus perfectly on a singular point as intended. A phase abberation exists when the EM rays which cross paths at a singular point are not all perfectly in phase as intended. We say they are out of focus. This is the case for the focal arc or beam contour everywhere except at the foci. The phase error of these lenses refer to the received phase error distribution across the array aperture.

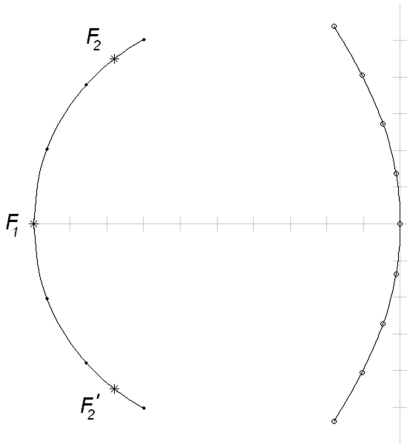

Figure 3.5: The geometry of a trifocal bootlace lens using an elliptical beam contour.

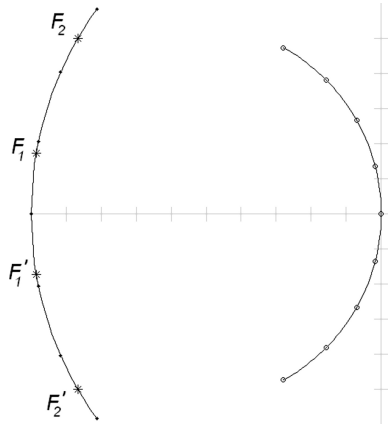

Figure 3.6: The geometry of a quadrifocal bootlace lens using an elliptical beam contour.

The rays transmitted from a non-focal beam port will not collimate at the desired wavefront in phase. We can compare the path lengths of each ray with the required path length of a reference ray. The difference is the phase error.

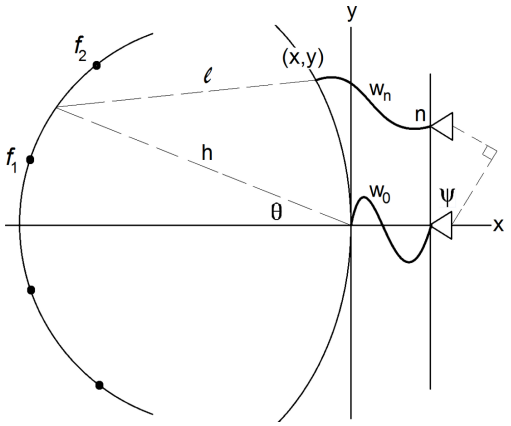

Figure 3.7: The lens geomeotry showing path lengths to an interfocal beam port.

Figure 3.7 shows the lens geometry with the rays traced from an arbitrary, non-focal point on the beam contour. This point makes an angle θ with the array contour centre and horizontal axis, known as the lens angle, and radiates a beam at a squint angle of ψ as shown in the figure. The two ray paths shown from the beam port to the desired wavefront are not equal in electrical length, and therefore have a phase error in relation to each other.

We will analyse a lens's phase error as a function of the lens angle θ and the array position. We choose the reference path as the path to the centre array element. Coordinates x and y represent any point on the array contour with a corresponding delay path w_n and element height n.
Then, the normalised pathlength error at any point on the array from a point $(-h\cos\theta, h\sin\theta)$ situated on the beam contour is

$$\begin{aligned} e =& l + w_n + \zeta\sin\theta - h - w_0 \\ =& \sqrt{(h\cos\theta + x)^2 + (h\sin\theta - y)^2} + (w_n - w_0) + \zeta\sin\theta - h \end{aligned} \tag{3.31}$$

Thus for a given θ we have the phase error as a function of ζ. The vector magnitude h is given by equation 3.29. For convenience we will express the phase error in degrees. Then, to scale the phase error we use:

$$E_{deg} = e \times \frac{L_1}{\lambda} \times 360^\circ \tag{3.32}$$

The phase error associated with each ray path will help define the performance of the lens. We will therefore analyse the lens parameters in light of their effect on the phase error.

J. Ruze described the error along the array aperture as a power series[9], he then provided optimising equations for the refocusing of the focal arc for various bifocal lenses. The focal arc was a circular arc centred at the middle of the array contour. For the lens which uses a linear array aperture he suggested the refocusing amount be

$$\epsilon_f = \frac{1}{2}(\alpha_2^2 - \theta^2)L_2 \tag{3.33}$$

where θ is the lens angle of a point that will intersect the refocused focal arc. Rotman and Turner implemented this equation for a trifocal lens, with the extra focal point on the axis of symmetry. Thus substituting $\theta = 0^\circ$, $\epsilon_f = L_1 - L_2$, and normalising to L_1, Rotman and Turner use the following equation for minimising phase errors:

$$\beta = \frac{2}{2 + \alpha_2^2} \tag{3.34}$$

The name "Rotman lens" is generally used to refer to all trifocal lenses[7], which allow for various α_2 and β values. However, lenses using the refocusing defined by equation 3.34 we call here "traditional" Rotman lenses. The term "refocusing" used by Rotman refers to an adjustment of the focal contour.

3.4 Analysis of the Lens Parameters

3.4.1 Introduction

The lens design equations leave several variables open for choice. These are listed in table 3.1. The lens equations have been implemented in Matlab to provide an analysis.

Table 3.1: Configurable lens paramaters

Parameter	Symbol
Number of array elements	A
Number of beams	B
Centre focal angle	α_1
Edge focal angle	α_2
Focal length ratio	β
Maximum scan angle	ψ_{max}
Lens angle ratio	γ
Centre focal length	L_1
Array element spacing	d_e
Focal arc ellipticity	ρ

We will now exaimine these parameters with respect to their effect on the lens geometry, and thereafter we examine their effect on the phase errors. These effects are summarised and a general design procedure is described.

3.4.2 The effect on lens geometry

We explore this for practical reasons, as the geometrical shape of the lens contours affect the implementation of the lens in manufacturable form. It is therefore desirable to modify the lens accordingly. Hansen[16] has done an analysis on the effect of parameters on the lens geometry, and we follow a similar approach here. For each parameter analysed, a figure showing the parameter's effect on the lens geometry is shown. The beam contour appears on the left of the figures and the array contour on the right. The locations of the ports are also marked. All units are scaled to the focal length L_1. The axes are plotted with unit lines, where each unit line represents a value of 0.1. Unless otherwise stated, the lens parameters are given as $\alpha_1 = 0°$, $\alpha_2 = 35°$, $\beta = 0.9$, $\psi_{max} = 40°$, $\gamma = 1.1$, $L_1 = 4\lambda$, $d_e = 0.5\lambda$, and $\rho = 1$. Parameters are first analysed on the trifocal lens, as this allows us to see the effect of β.

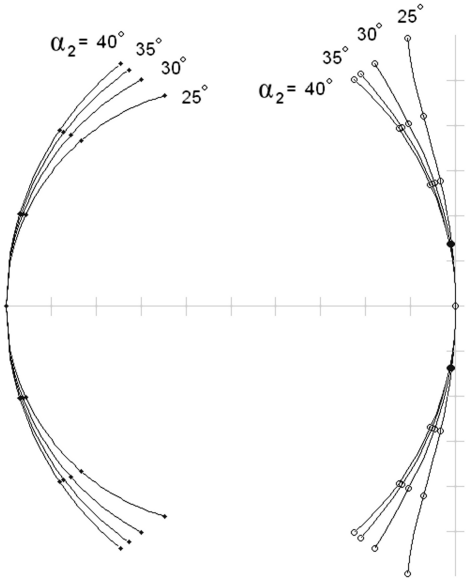

Figure 3.8: The edge focal angle, α_2, affects the curvature of both the beam and array contours.

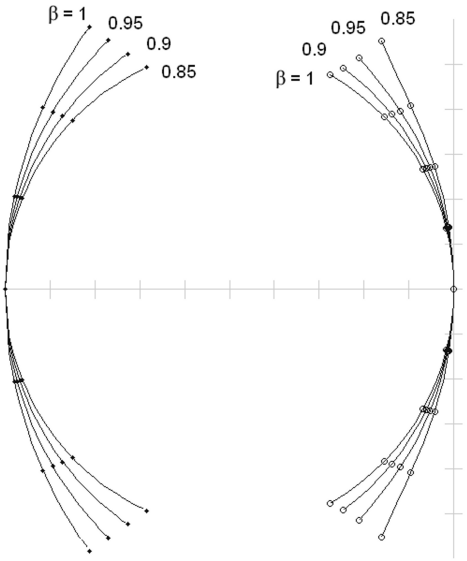

Figure 3.9: The focal ratio, β, affects the curvature of both the beam and array contours.

Figure 3.8 shows the effect of varying the edge focal angle, α_2, on the lens geometry. As α_2 is increased, the beam contour curvature opens while the array contour curvature closes. Port positions remain largely unchanged along the lengths of both contours. Since α_2 represents a point on the beam contour with perfect focus, varying α_2 will also influence the phase aberration experienced on the rest of the beam contour.

Increasing the focal ratio, β, has a similar effect to that of increasing α_2; The beam contour curvature opens and the array contour curvature closes. This effect is shown in figure 3.9. Again, port positions remain largely unchanged along the lengths of both contours. Since both α_2 and β have the same effect on the contours, various pairs of α_2 and β can give similar geometry. However, the phase error, transmission line path length, and foci positions do vary. Performance regarding the phase errors is covered in the next section.

Figure 3.10 shows the geometry of a quadrifocal lens and the effect of changing the centre focal angle α_1. A similar change in α_2 has the same effect. Only the array contour curvature changes as the focal ratio is limited to unity.

The maximum scan angle, ψ_{max}, is usually given as a specification for design. The outer most beam port on the beam contour is responsible for transmitting or receiving the beam at the desired maximum scan angle, and the angle which this beam port makes with the centre of the array contour is related to ψ_{max} by the

angle ratio, γ. Varying ψ_{max} lengthens or shortens the beam contour accordingly, and repositions all off-axis beam ports since they are evenly spread on the beam contour. Figure 3.11 shows the effect on the lens geometry when ψ_{max} is altered.

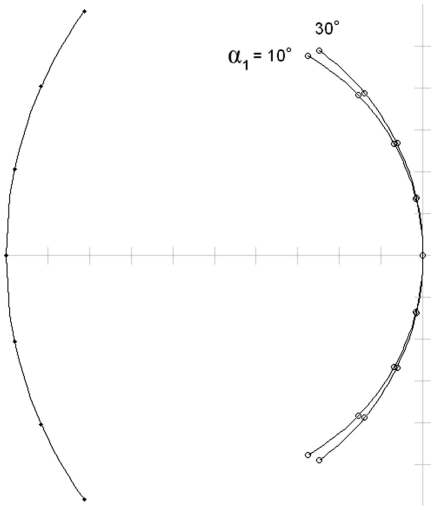

Figure 3.10: The effect of changing the centre focal angle on a quadrifocal lens.

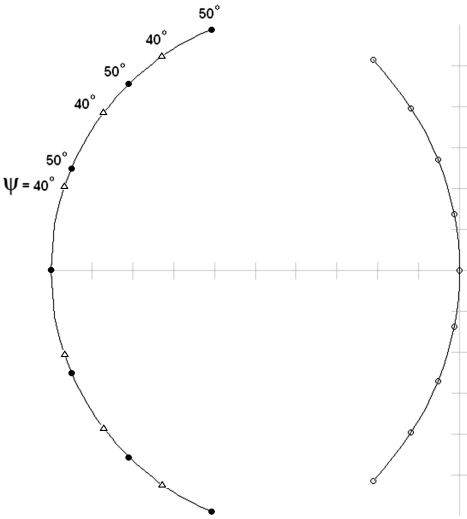

Figure 3.11: The effect of changing the maximum scan angle.

A moderate change in the beam contour's ellipticity, ρ, is almost unnoticeable whereas the phase errors are largely affected. Thus, the interest in ρ is in its phase errors which will be discussed in the next section. Recalling equation 3.3 we have

$$\zeta = \frac{N\gamma}{L_1}$$

ζ is an indirect parameter described by Hansen which extends its use to the phase and amplitude error along the array contour. Although not directly stated by Hansen, ζ, practically speaking, represents the length of the array contour since its dependencies are all the variables which determine the length of the array contour. N is the height of an array element on the vertical axis of the array aperture. It is determined by the number of elements used and the element spacing d_e. ζ is maximum where N is maximum, given by

$$N_{max} = \frac{d_e(A-1)}{2} \tag{3.35}$$

for A equal to an odd number, or

$$N_{max} = \frac{d_e A}{2} \tag{3.36}$$

for A equal to an even number, where A is the number of array elements.

ζ is directly proportional to the element spacing. Figure 3.12 shows the lens geometry for 0.5λ and 0.6λ element spacing. The curvature of both contours remains the same. However, the array ports position moves further up the length of the array contour as d_e increases, as does the total array contour length. Furthermore, the separation between the array ports, d_p, increases. An array port spacing beyond a certain value will introduce grating lobes inside the lens[8], given by

$$d_p = \frac{1}{1 + \sin\psi_{max}}\lambda \tag{3.37}$$

Array port spacings should be kept below this value. A maximum scan angle of 30° limits d_p to 0.66λ, and a maximum scan angle of 60° limits it to 0.53λ. The array element spacing d_e is usually also limited to prevent grating lobes in the scan space.

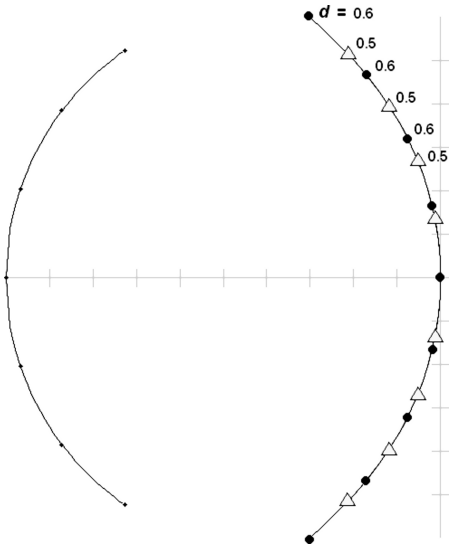

Figure 3.12: The effect of the array element spacing on the lens. d is given in wavelengths.

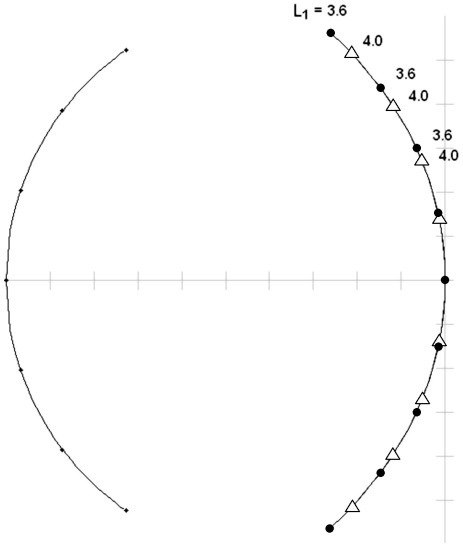

Figure 3.13: The effect of increasing the lens width, L_1.

Now, γ is the angle ratio which relates any lens angle θ of a beam port to its corresponding beam angle ψ, and is given by equation 3.2 as

$$\gamma = \frac{\sin\psi}{\sin\alpha_2}$$

Figure 3.14 shows the effect of γ on the lens geometry. The port positions of both contours are altered by a change in angle ratio. Corresponding to equation 3.3, ζ increases in proportion to γ. There is no change in either contour curvature.

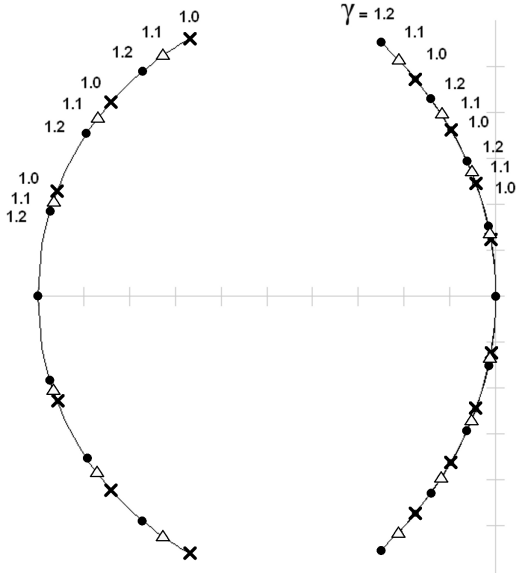

Figure 3.14: The effect of the angle ratio on the lens geometry.

Although the focal angle stays unchanged, the beam port positions move closer together along the beam contour with an increase in γ, while the array ports are spread further apart on the array contour. This shortens the beam contour length and increases the array contour length. γ can then be used to avoid grating lobes within the lens.

Lastly, ζ is also dependent on the scaling factor of the lens: the focal length L_1. L_1 is the distance from the array contour centre to the first focus, and is inversly proportional to ζ, as seen in equation 3.3. Figure 3.13 shows that an increase in the focal length draws the array ports closer together on the array contour. The beam ports position remained unchanged as does the curvature of both contours. However, the plot in figure 3.13 is normalised to L_1, so in reality an increase in L_1 only causes the contours to move further apart and the beam contour to scale in size accordingly, as the beam port positions are dependent on the angle they make with the array contour centre. Thus the array ports are only moving closer together in relation to the lens size, and not in physical dimension. In physical dimension, it is the beam ports which spread further apart as L_1 increases.

The effect of parameters ψ_{max}, d_e, L_1, ρ, and γ on a trifocal lens, as previously shown, is exactly the same for the case of a quadrifocal lens. The difference is that β is restricted to unity, and focal angles α_1 and α_2 only affect the array contour. Various quadrifocal lenses essentially have about equal beam contour curvatures.

3.4.3 The effect of the parameters on the phase error

The phase error of a lens was defined in section 3.3.3. We have analysed the effect that the lens parameters, listed in table 3.1, have on the lens geometry. We will now analyse their effect on the phase error.

It is convenient to analyse the phase error as a function of the lens angle, θ, and the position on the array contour. Recall that θ is the angle made between an arbitrary point on the beam contour and the centre point of the array contour, as shown in figure 3.7. ζ is a parameter of indirect utility as defined in the previous section, and represents the position along the array contour because ζ is equal to zero at the centre of the array contour and is maximum at the contour's end points. From equation 3.3 we get that ζ_{max} is given by

$$\zeta_{max} = \frac{N_{max}\gamma}{L_1} \tag{3.38}$$

where N_{max} is given by equation 3.35 or 3.36 depending on whether the number of array elements used are even or odd. The parameters listed in table 3.1 which only affect the array contour length, or ζ, only influence where the phase error cuts off and not the phase error itself.

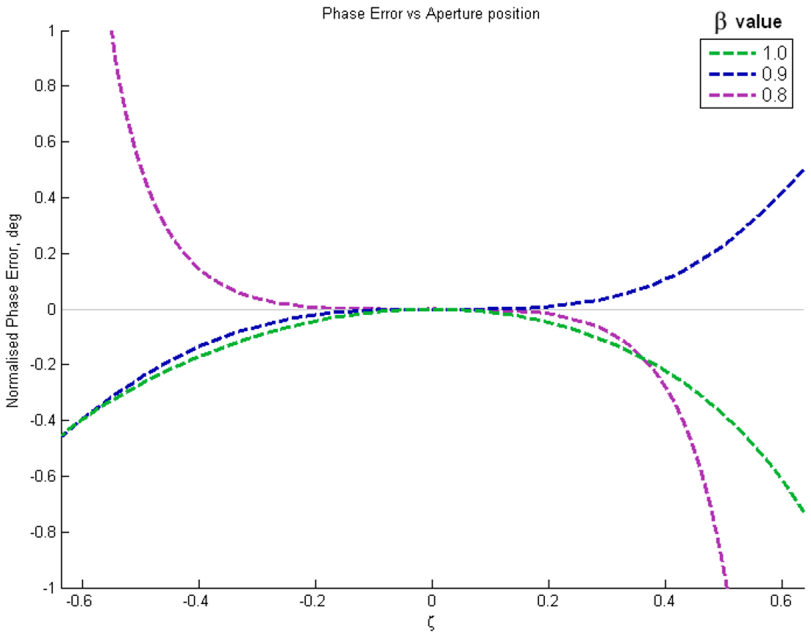

Figure 3.15: The phase error of a trifocal lens for different values of β, where $\alpha_2 = 35°$ and $\theta = 17.5°$.

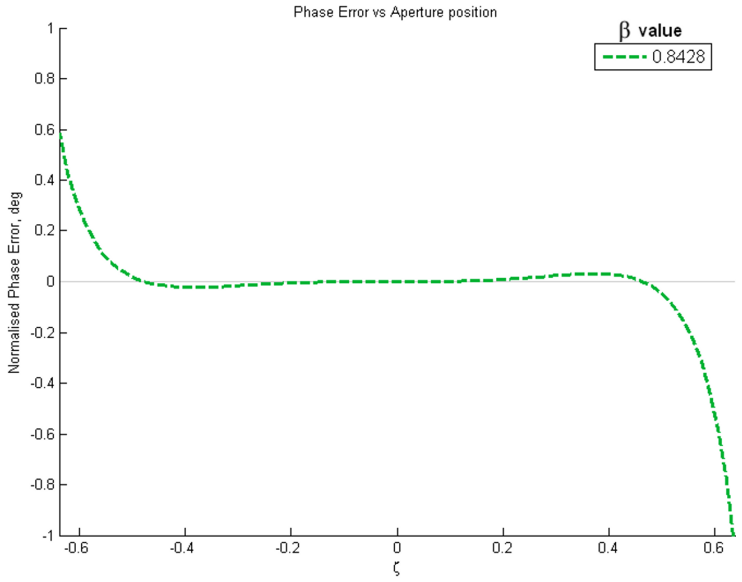

Figure 3.16: The phase error of a Rotman lens in the "traditional" sense. $\alpha_2 = 35°$ and $\theta = 17.5°$.

Figure 3.15 shows a plot of the phase error verse ζ of a trifocal lens for three different values of β. The phase error is given in degrees and is normalised to L_1/λ, and must again be multiplied by this same value to get the actual phase error. For this plot, the lens parameters are $\alpha_2 = 35°$, $\psi_{max} = 40°$, $\gamma = 1.1$, $L_1 = 4\lambda$, $d = 0.5\lambda$, and $\rho = 1$. The lens angle which corresponds to these phase errors is chosen to be midway between the foci, $\theta = 17.5°$. It is seen that the phase errors worsen as ζ increases. The ζ cut-off for the lens parameters is $\zeta_{max} = 0.55$. A smaller aperture, therefore, gives better phase error results.

By selecting various values for α_2 and β, it is clear that their influence on the phase errors are dependent on each other. When Rotman and Turner applied Ruze's refocusing equations to the trifocal lens, they suggested that a reasonable optimum is attained when α_2 and β are linked by the equation 3.34. However, Hansen states that "an optimum β exists only for one range of ζ and one ray angle"[16]. Figure 3.16 shows another phase error plot for the same lens angle and parameters given in figure 3.15, but now the lens is refocused by equation 3.34 so that $\beta = 0.8428$. The phase error is improved, but only for a fixed range of ζ.

For any limitation on the phase error, the β of figure 3.16 allows for a larger aperture compared to the arbitrary β values chosen in figure 3.15. However, slight variations in this β value can improve the lens depending on ζ_{max}. To illustrate we first look at a wider range of angles.

The normalised phase error is shown in figure 3.17 as a contour plot over all

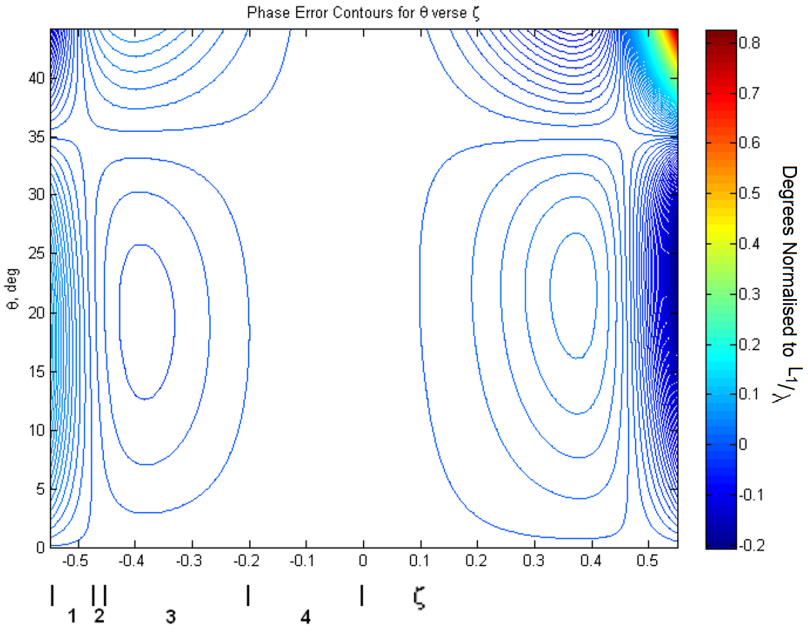

Figure 3.17: The phase error contour plot for a trifocal lens.

values of ζ and positive θ in range. Due to the lens symmetry, it is sufficient to only plot the positive values of θ. Here, the plot ends at the ζ_{max} value of 0.55. The foci at lens angles 0° and 35° can be seen. Recall that the phase errors at $\zeta = 0$ are also zero because that is where the reference phase is, and to which all other phases are compared. Figure 3.17 indicates four numbered regions beneath the plot. Although, in this case, the regions shown in the figure are symmetrical about $\zeta = 0$, the phase errors are not.

In region one the phase errors grow exponentially worse as ζ increases in magnitude, and in region two the phase errors become zero and reverse sign at a particular value of ζ, as can be seen in figure 3.16. Region three falls between the phase error nulls and displays a phase error which has its maximum towards region two. Lastly, region four is in the middle of the aperture where the phase errors are negligible in comparison. A lens which only uses region four as the array contour may be realised, however the lens will need to be large in scale and the spillover loss will be severe. The contour plot in figure 3.17 has a β value of 0.843 as given by the refocusing of equation 3.34. As β increases from this value, region two moves higher up on the aperture and region three's errors increase and become progressively unsymmetrical. As β decreases from the refocused value, region two moves down the aperture. This causes the phase errors of region three to reduce and that of region one to increase. Results are similar when α_2 is set to a different value and the refocused β

is adjusted. As a design technique, for a given α_2, one can start with a refocused β as per equation 3.34 and adjust the value depending on the ζ_{max} requirements of the lens.

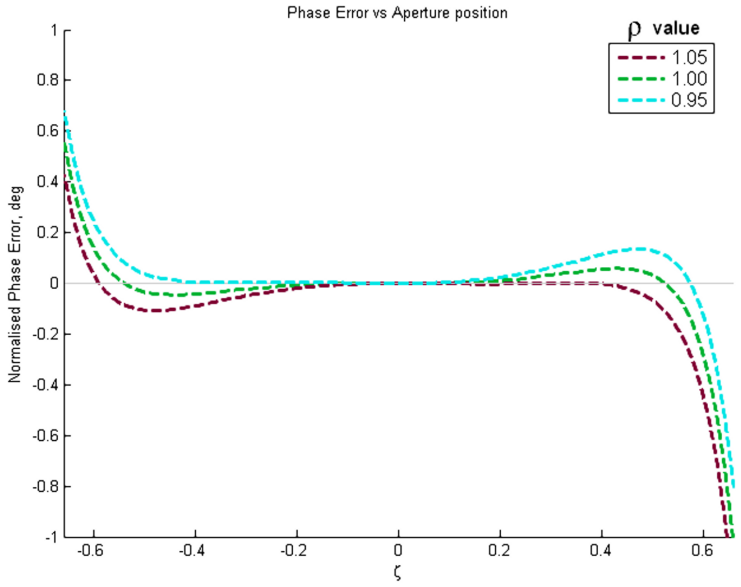

Figure 3.18: The phase error of a trifocal lens for different values of ρ, where $\beta = 0.85$, $\alpha_2 = 35°$ and $\theta = 17.5°$.

The phase errors beyond the edge foci of the lens become progressively worse and can be limited by adjusting the maximum θ value. The maximum θ is the lens angle that corresponds to the edge beam port, and can be lowered by either increasing the angle ratio γ, or by decreasing the scan angle ψ_{max} as shown in the previous section. However, γ also influences ζ_{max}, whereas ψ_{max} is usually defined by a set specification.

The variables of ζ_{max}, given by equation 3.38, do not actually change the phase errors, they only set the cut-off point of the existing phase errors. We can essentially crop out the phase errors of the contour plot given in figure 3.17 by limiting ζ_{max} and θ_{max}. α_1, α_2 and β affect the phase errors for every angle θ, as does the beam contour ellipticity ρ. The effect of the ellipticity is shown in figure 3.18. Note that when ρ is unity the beam contour is circular. The effect of ρ on the phase errors of a lens are not well defined. Figure 3.18 depicts the phase error when the beam contour deviates from its previously circular shape. ρ greatly affects the symmetry of the phase errors about the aperture centre. It is found that for those values of θ where the phase errors are unsymmetrical, ρ may be adjusted to restore symmetry, however, not for all θ simultaneously. A subtle adjustment in ρ can slightly improve

the overall phase errors of a lens. Hansen states that the "use of an elliptical beam port arc is usually not warranted except for large lenses"[16].

We may stipulate that a lens is as good as its worst phase error, and sweep certain parameters until they are optimised. This is appropriate for lenses with more than four beams, else the beam ports are just placed on the foci. Since the number of beams are usually given by the specifications, we only need to sweep over the values of θ which correspond to those beam ports. The relationship between α_1, α_2 and β predominantly determine the phase errors of a lens. We thus start by sweeping these parameters. For every parameter sweep we record the overall worst phase error in range and compare these to find the optimal values.

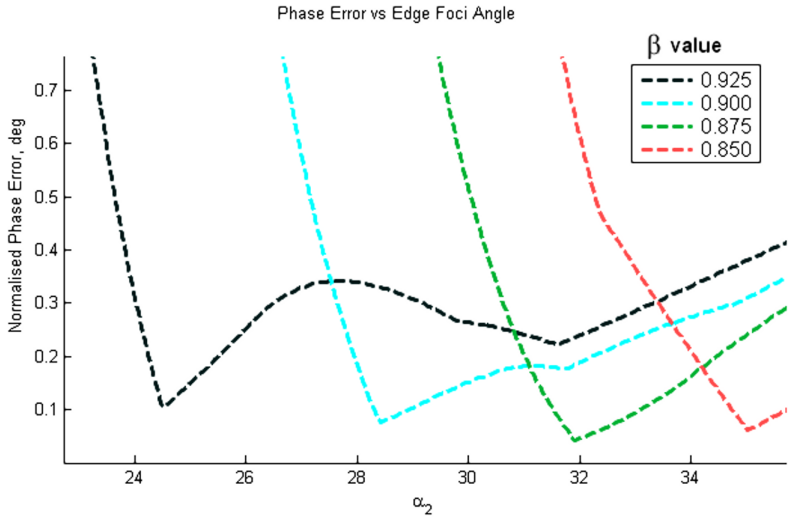

Figure 3.19: Parameter sweep of the edge focal angle for a given β.

Figure 3.19 shows the worst phase errors of a trifocal lens for all beam angles verse α_2, for different β values. A clear minimum is found for each curve, some better than others. These best α_2 - β pairs are dependent on ζ and therefore do not agree with the refocusing of equation 3.34 given by Rotman and Turner. However, they are near and serve as a reasonable estimate.

Now for the same lens parameters but for a quadrifocal lens, we sweep α_1 and α_2 to find the least phase errors. This gives the best normalised phase error of the quadrifocal lens a value of $0.403°$ for an $\alpha_1 \approx 16°$ and an $\alpha_2 \approx 33°$. The trifocal lens achieved a best normalised phase error of $0.043°$ for a $\beta = 0.875$ and an $\alpha_2 \approx 32°$. The trifocal lens therefore holds about a tenfold improvement over the quadrifocal lens regarding phase errors. However, for the trifocal lens, as β increases towards

unity, the best phase error rapidly escalates so that at $\beta = 1$ it has a value of about 0.55°. Therefore the quadrifocal lens should be used if equal focal lengths are desired. This is the case if the beam contour should be circular and centred on the array contour origin. However, for any other focal ratio, a trifocal lens is preferable.

The phase errors that were given are in degrees and have been normalised to L_1/λ. Thus L_1 directly scales the phase error of a lens, meaning larger lenses will have a degraded performance. Phase errors worse than about 0.1λ or 36° will begin to adversely affect the side lobe levels of an array[7], and must therefore be kept below this value. Increasing the number of elements only requires an increase in L_1, and therefore the normalised phase errors remain the same for large lenses. If phase errors of up to 5 degrees are considered negligible, a trifocal lens designed for minimum phase errors can have to about 500 elements at a maximum scan angle of 30°, or about 200 elements at a maximum scan angle of 50°. This comprises most practical lenses[3].

3.5 General Design Procedure

Here we provide a brief summary of the parameter analysis and a general design procedure for three and four foci bootlace lenses. Table 3.2 outlines the effects of the parameters on the lens geometry and phase errors, given the parameter values are increasing.

The specification of a lens usually defines the number of elements A, the number of feed ports B, the element spacing d, and the maximum scan angle ψ_{max}. Unless equal focal ratio's are required, a trifocal lens should be used. Focal angles α_1 and α_2, the focal ratio β, angle ratio γ, and focal length L_1 should be estimated so that the beam contour height is slightly below the array contour height. This is to prevent excessive spillover loss.

Next, α_2 and β for trifocal lenses, or α_1 and α_2 for quadrifocal lenses, should be swept for minimum worst phase error at the beam ports. If the new values after the parameter sweep cause the beam contour height to be above the array contour's, then adjust the other parameters to fix this and repeat the α_1-α_2 or α_2-β sweep. Small adjustments in the beam ellipticity can then be applied for final optimisation in the phase errors.

This procedure is just general and not necessarily optimal. When the lens is implemented in a manufacturable form, further restrictions might be required on the lens, such as a specified distance between feed ports. Table 3.2 can be used to experiment on further geometries.

Table 3.2: The effect of an increase of the lens parameters, regarding the geometry and phase errors of the lenses.

Parameter	Trifocal lens geometry		Quadrifocal lens geometry		Phase errors, both lenses
	Beam contour	Array contour	Beam contour	Array contour	
A		increases length		increases length	
B					
α_1				opens curvature	affects all errors
α_2	closes curvature	opens curvature	opens curvature		affects all errors
β	closes curvature	opens curvature			affects all errors
ψ_{max}	increases length		increases length		increases θ_{max}
γ	decreases length	increases length	decreases length	increases length	decrease θ_{max} & increases ζ_{max}
L_1		increases length		increases length	increases ζ_{max}
d_e		increases length		increases length	increases ζ_{max}
ρ	opens curvature		opens curvature		symmetry

3.6 Conclusion

In this chapter the design equations for trifocal and quadrifocal lenses were derived for linear antenna array apertures. Trifocal lenses have an extra degree of freedom over quadrifocal lenses allowing them to achieve smaller phase errors, unless equal focal lengths are desired. The effect of the available parameters on the lens geometry and phase errors have been investigated. Parameter sweeps of the focal angles and focal ratio reveal that a single minimum in the phase errors exist, and the traditional Rotman lens has phase errors which are near but not on this minimum. The optimised phase errors are practically negligible for most practical lenses.

Table 3.2 summarise the effects of the lens parameters and serves as a reference. In the following chapter we investigate the implementation of these lenses in waveguide.

Chapter 4

Implementing the Lens in Waveguide

4.1 Introduction

In the previous chapter we derived the design equations of 3 and 4 foci bootlace lenses, and analysed the effect of the parameters on the lens geometry and respective phase errors. The lens equations provide a blueprint of the port positions, in this chapter we investigate the practical implementation thereof in waveguide.

The polarisation of the electric field in the waveguide determines what type of ports can be used. Two categories are investigated and compared. The performance of a vertically polarised horn, as it is used in these lenses, is examined. It is also critical that the phase centre of the horn is known so that they may be positioned exactly. A better amplitude taper across the array ports is given for feed horns pointed in the direction of the array contour centre[16]. However, if the horns are closely positioned on a circular arc they overlap or leave obscure gaps, a solution uses horns of different sizes. Lastly, the sidewalls and spillover loss of a Bootlace lens is defined, and a general design procedure to implement the lens in waveguide is provided.

4.2 Waveguide ports

4.2.1 Vertical verse horizontal polarisation

Bootlace lenses which are implemented in waveguide can be placed in two categories; those which have their electric field vertically polarised and those which have it horizontally polarised. The difference relates specifically to the ports. To use these

lenses for RADAR application, it is essential for beam ports to be reasonably isolated from each other. Energy coupling into a beam port due to a mismatch at the port, reflections within the lens, or mutual coupling between the beam ports all contribute to the "noise floor" of the lens. This noise can prevent the recognition of received signals. Therefore, these factors are required to be minimised to the improve the performance of the RADAR device.

Waveguide horns are typically used as the beam ports. Coupling to the waveguide horn requires a coaxial transition, which typically gives about 12% bandwidth[5]. The bandwidth can be improved by using certain parasitic elements such as a waveguide iris or tuning screw. Horns are flared, and can be tapered to allow for a more gradual transition between the port and parallel plate region, giving a better impedance match[4]. The lens structure is electrically large. With the focal length L_1 given by four wavelengths or more, the array ports approximately fall within the beam ports' farfield. We may therefore analyse the beam ports as separately from the array ports.

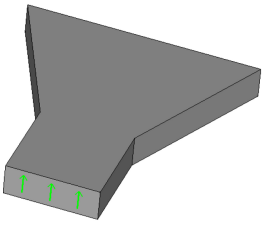

Figure 4.1: An H-plane horn used for vertical polarisation, with the electric field direction shown.

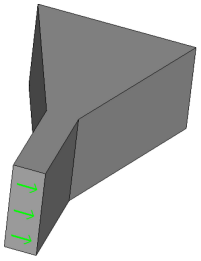

Figure 4.2: An E-plane horn used for horizontal polarisation, with the electric field direction shown.

The difference between vertically and horizontally polarised horns is illustrated in figures 4.1 and 4.2. Figure 4.1 shows an H-plane horn which is used for vertically polarized lenses, and figure 4.2 shows an E-plane horn which is used for horizontally polarised lenses. In a rectangular waveguide the cutoff frequency for each mode is given by[18]

$$f_{c_{mn}} = \frac{1}{2\pi\sqrt{\mu\epsilon}}\sqrt{(\frac{m\pi}{a})^2 + (\frac{n\pi}{b})^2} \tag{4.1}$$

where a and b are the cross-sectional dimensions of the waveguide. Constants μ and ϵ are the respective magnetic permeability and electric permittivity of the material in which the energy is propagating. The dominant mode used in these horns is the TE_{10} mode. In order for this mode to propagate, the horn dimension running

perpendicular to the electric-field must be greater than half a wavelength. The horn dimension running parallel to the electric-field vector should remain below half a wavelength to avoid the TM_{11} mode. It is usually recommended that the horn aperture not be flared greater than a wavelength as this will support the the TE_{20} mode causing the energy to be overmoded[19]. However this not always the case unless there exists a discontinuity which supports the overmoding. It is advantageous to flare the horn to an aperture width of over a wavelength as this increases the horns directivity[6]. Energy in the parallel plate region propagates as a TEM wave when the electric-field is vertically polarised, and as the TE_1 mode when it is horizontally polarised.

There is a geometrical limitation concerning the array ports. Recalling equation 3.37, array elements have their spacing between them restricted to typically ± 0.6 of a wavelength, if grating lobes within the lens are to be avoided[8]. The position of an array element on the array aperture is directly related to the position of the array port on the array contour to which the element is connected. As seen in the previous chapter, the angle ratio γ is the only variable which affects the array port spacing without also affecting the the element spacing on the array aperture.

Table 4.1: The distance between the array ports.

	Distance from previous port (λ)		
Port	$\gamma = 1.0$	$\gamma = 1.1$	$\gamma = 1.2$
Centre	-	-	-
1st	0.5002	0.5502	0.6003
2nd	0.5052	0.5569	0.6090
3rd	0.5158	0.5714	0.6282
Edge	0.5336	0.5963	0.6628

Table 4.1 shows the distance between array ports for three different values of γ. These values are for a lens with $\alpha_2 = 35°$, $\beta = 0.9$ and $d = 0.5\lambda$. The spacing increases from the centre to the edge ports. Since the H-plane horn requires a width of over 0.5λ to support the fundamental mode, it is impractical to use H-plane horns for the array ports. An array port spacing of at least a wavelength is required before H-plane horns can be appropriately used with a flared aperture. This much separation between array ports is possible if γ is heavily escalated, but results in a large lens with grating lobes.

E-plane horns are not restricted by this spacing since half a wavelength is sufficient to support the ports. E-plane horns can therefore be utilised along the array contour. Instead of horns, lenses with the electric field vertically polarised use coaxial probes which extend into the waveguide as shown in figure 4.3. A conducting

wall is placed behind the probe which is called the array backwall. The coaxial centre conductor is capacitively coupled to the waveguide allowing an impedance match at a single frequency.

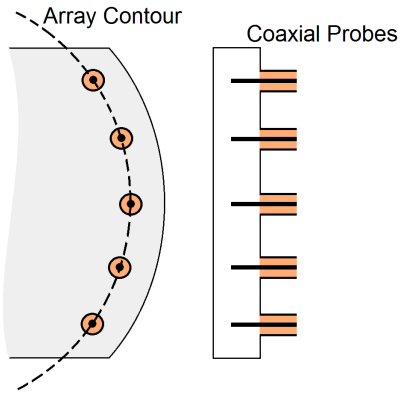

Figure 4.3: The top and side view of the coaxial probes used as the array ports. A conducting wall is positioned behind the probes.

A waveguide lens that uses coaxial probes, instead of horns, for its array ports is more compact. The phase centre of a coaxial probe is exact and does not change with frequency. However, a horn has its phase centre somewhere in between the aperture and apex, which also changes with frequency[20]. These lenses are designed for certain EM ray path-lengths, thus accurate port phase centres are essential to avoid unnecessary phase errors. The phase centre of a horn can be calculated[20], which could be implemented in software to be used in conjunction with the lens equations.

Another method is to find the horn's phase centre by simulation. However, this requires a trial and error approach. It is therefore convenient to use coaxial probes as the array ports. Generally, a lens is designed for more array elements than beam directions[3]. This allows for a larger separation between beam ports, which accommodates horns with wider apertures and therefore better directivity. It also allows the use of H-plane horns. We will therefore use vertically polarised lenses with H-plane horns for beam ports and coaxial probes for array ports. Coaxial probes cannot be used for the beam ports due to the previously mentioned isolation requirement between these ports.

4.2.2 Horn Implementation

Waveguide horns used for these lenses are usually of the form shown in figure 4.4. A coaxial to waveguide transition feeds the horn. A taper can be applied to the

horn to provide a gradual impedance change. Figure 4.5 shows a compact version of the same horn where the rectangular section is excluded from the horn. This can shorten the length of the horn up to 3 times.

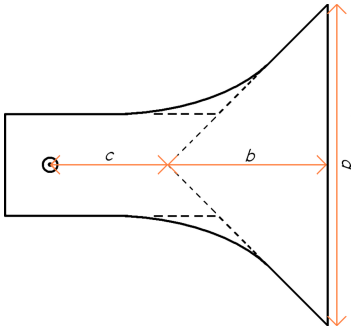

Figure 4.4: A waveguide horn with a coaxial transition

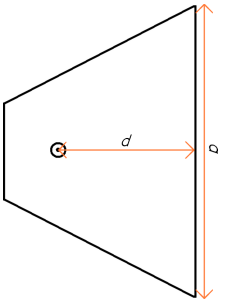

Figure 4.5: A compact version the waveguide horn of figure 4.4

It is desired to flare these horns to an aperture width well over a wavelength to increase their directivity. Since they will then accommodate higher order modes, it is possible for these ports to become over-moded and cripple a lens's performance[21]. A method used to avoid this possibility splits the port into two separate horns and connects them with a magic-T[19]. A total aperture width up to two wavelengths is then possible without supporting higher order modes.

We will continue to simulate both horns described in figures 4.4 and 4.5, as it pertains to the implementation of the lens. The transition from coaxial to waveguide for both horns is a coaxial probe shown in figure 4.6.

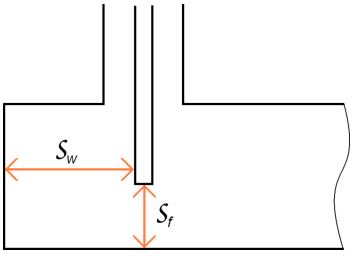

Figure 4.6: The coaxial to waveguide transition of the ports.

The coaxial probe is tuned to match the impedance at a single frequency by using two parameters; the separation between the coaxial centre conductor and the conducting floor, s_f, and the separation between the coaxial centre conductor and conducting wall, s_w. Using parameters s_f and s_w we are able to match the horns to a single

frequency. Figure 4.7 shows the reflection coefficient plots for these two horns, matched to 3.5GHz. For our purposes we label the horn in figure 4.4 as the normal horn, and the horn in figure 4.5 as the short horn. They perform equally with a 14% bandwidth at -15dB or 7.4% bandwidth at -20dB.

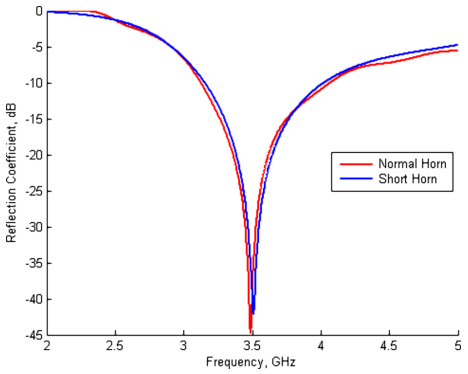

Figure 4.7: The reflection coefficents for both horns, matched to 3.5GHz

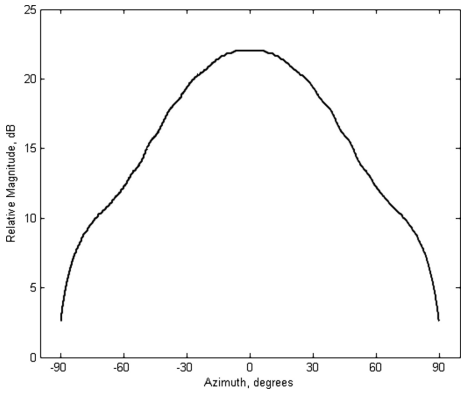

Figure 4.8: The radiation pattern given by the short horn

Where the wavelength is $\lambda = 85.71$mm, the waveguide height is chosen to be 30mm and the port back-wall widths are chosen as 65mm. This follows from equation 4.1, so that the height is smaller than half a wavelength and the width is greater than half a wavelength. Unless otherwise stated, for these simulations we used the dimensions $a = 1.5\lambda$, $b = 2\lambda$, $c = 0.2\lambda$, and $d = 0.75\lambda$ for figures 4.4 and 4.5.

We can manually find the phase centre of a horn by looking at the phase of the electric field along a circular arc in a simulation. The arc's centre point is shifted until the phase deviation of the radiated electric field is at a minimum. For both horns, it is found that even at this minimum, the phase still deviates by up to about 4 degrees. For aperture widths of 1.5λ, the normal horn has its phase centre situated at about 0.25λ from the aperture towards the apex, and the short horn's is is situated at about 0.19λ toward the apex. These values increase as the aperture widths increase.

Figure 4.8 shows a simulation plot of the relative magnitude of the energy radiated by the short horn port for a 180° azimuth sector. This was done by simulating the electric field along a half circle of about 5 wavelengths in radius and centred at the horn's phase centre. The normal horn's radiation pattern is similar. It is desirable for these horns to produce narrow beam widths as this reduces the spillover loss, and provides an amplitude taper across the array aperture which has lower side lobe levels.

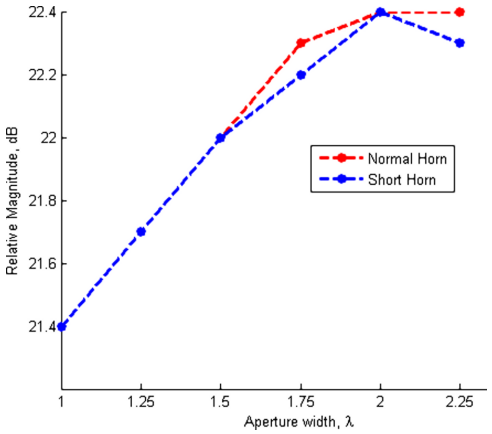

Figure 4.9: Comparison of the relative magnitude of the horns' main beam

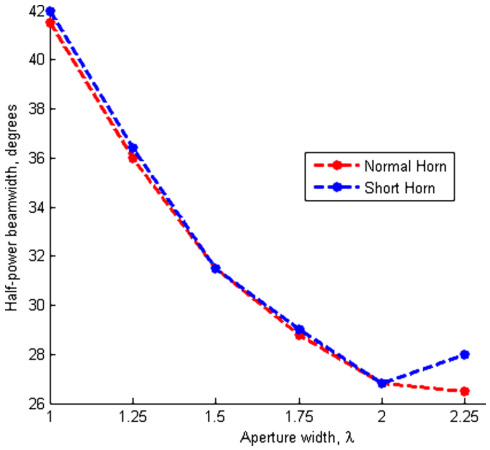

Figure 4.10: Comparison of the half-power beamwidth of both horns

Figure 4.9 compares the maximum magnitude achieved by the two horn types for various aperture widths, and figure 4.10 compares their half-power beam widths. They perform similarly, with the short horn reaching maximum gain and minimum beam width earlier than the normal horn and at an aperture width of 2λ. The separation between beam ports will rarely allow for aperture widths greater than two wavelengths.

For the normal horn, it is found that changes in variable b up to a wavelength from the value (2λ) used in the graphs only have a subtle impact on the beam magnitude, beam width, or reflection coefficient. For the short horn, variable d can differ by about a quarter wavelength from the value (0.75λ) used in the plots before a deterioration in performance is noticeable. For both horns, larger aperture widths are first affected.

The performance of these horns are therefore not sensitive for small to moderate variations in dimensions b and d. The horns perform the same, but the short horn has the advantage of being more compact. Therefore we use the short horn in our lens designs.

4.2.3 Port positioning on the beam contour

The beam contour is usually circular or elliptical. It may be convenient to place equally sized horns with known phase centres along it, with their axes perpendicular to the curve of the contour. However, for a better amplitude taper across the array ports, the horns' axes should go through the origin of the array contour instead[16]. This is only the case when the focal lengths are equal ($\beta = 1$), and is therefore an advantage of the quadrifocal lens. For the trifocal lens when $\beta \neq 1$, standard sized

horns pointed at the array contour's origin will either overlap or leave obscure gaps between them as shown in figure 4.11.

We would require an approach that uses different horn sizes and customises the horn shape to the lens. One such approach uses the geometry as shown in figure 4.12.

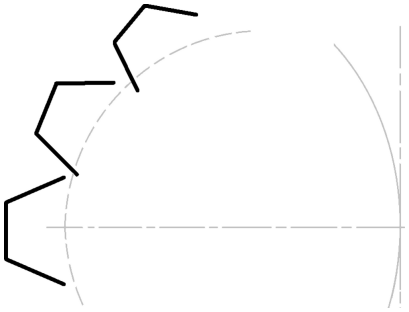

Figure 4.11: Positioning equal sized horns onto the beam contour which do not lie normal to the contour.

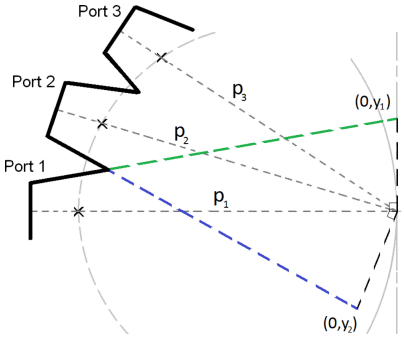

Figure 4.12: A geometrical method used to customise horn sizes to the beam port.

For each beam port, we start with a line drawn from the phase centre to the origin (the origin is taken as the array contour's origin). The horizontal axis of each port lies on their respective line. The port backwall with predefined width is marked for each port, a distance p_n from the origin, where n denotes the port number. Now starting with the centre beam port (port 1 in the figure), we draw a line from the top edge of the backwall to the coordinate $(0, y_1)$ as shown in green. For the next port (port 2 in the figure) we do the same, but from the bottom of the backwall to the coordinate $(0, y_2)$ as shown in blue. The aperture of the ports is then taken where these two lines intersect.

Is it essential that the beam ports are symmetrical about their own axes, otherwise the phase centre will be out of position. This symmetry condition of each port is enough to conclude the remaining ports. Variables y_1 and y_2 are then used to control the aperture widths for all ports. This method does not allow for all ports to have the same aperture width, although variations are small. A Good starting value for y_1 and y_2 is about half the height of the array contour. Values for p_n need to be chosen in conjunction with y_1 and y_2 so that the horns phase centre is positioned correctly. A focal ratio of one means all ports are already pointed to the origin and equal sized horns can be used. As the focal ratio decreases ports become increasingly unequal in size and it becomes difficult to correctly position all the phase centres.

4.3 The lens sidewalls

The lens design equations do not define a closed structure, but instead leave a gap between the beam and array contour edges as shown in figure 4.13. These are called the lens sidewalls. The energy radiated from a beam port towards the lens sidewalls is the spillover loss. Not only is the energy wasted but reflections off the lens sides result in unwanted coupling[21].

Two methods commonly used to dampen reflections off the lens sidewalls is the employment of either an absorbing material, or ports with matched loads - known as dummy ports. If space permits, it is recommended to use a curved contour for the sidewalls, as shown in figure 4.14, instead of a straight line[21]. This allows more dummy ports and positions them opposite each other so that the spillover energy entering the sidewalls are absorbed multiple times before reflecting back into the lens.

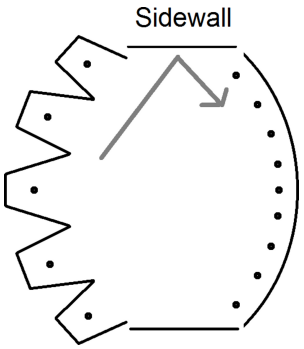

Figure 4.13: A waveguide lens with the straight line sidewalls shown.

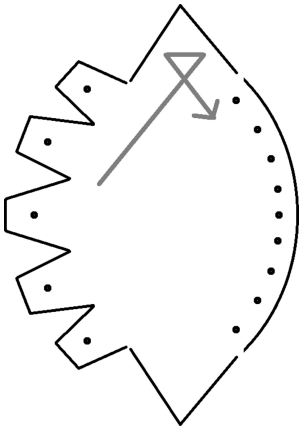

Figure 4.14: A waveguide lens using extended sidewalls.

4.4 Design Procedure

Here we summarise a design procedure for implementing a lens in waveguide for vertical electric-field polarisation. This follows from the geometrical design procedure in chapter 3.5, which gives the relative positions of the port phase centres.

First we establish the waveguide dimensions from the desired bandwidth. To avoid overmoding the ports, as indicated by equation 4.1, the height of the waveguide should be chosen as approximately a third of the upper frequency wavelength. The backwall widths of the horns should be chosen at about 0.6λ of the lower frequency. Then we construct the beam port horns using the method illustrated in figure 4.12.

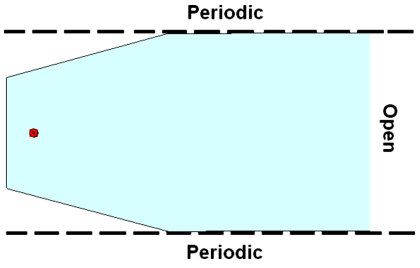

Figure 4.15: The CST model used to match a beam port.

The parameters y_1, y_2, and p_n must be configured so that the phase centres of all ports lie on the exact position given by the geometrical design. We accomplish this by simulating the phase data on an arc which is centred at the geometrical port and drawn through the array contour's origin. The beam is positioned correctly if the phase deviation is at a minimum.

With the horn dimensions known, parameters s_w and s_f as shown in figure 4.6 can be tuned to match the horn at the centre frequency. These lenses are electrically large resulting in long simulation times. Since the beam and array ports are only within each other's farfield, we can simulate them separately. Furthermore, the ports along a contour can be approximated as periodioc which further reduces simulation time. Figure 4.15 shows a beam port in CST where the top and bottom boundaries are periodic, and the end boundary is left open so that it doesn't interact with the port. The validation of this method is given in the following chapter.

A similar approach is taken for the array ports which are also matched to a single frequency using parameters s_w and s_f. The port is isolated with two adjacent ports shown in figure 4.16. The distance between the array ports is important. A symmetry plane further reduces simulation time. lastly, we terminate the lens sidewalls by either using dummy ports or an absorbing material.

4.5 Conclusion

There are two categories in which to implement a lens in waveguide. The first uses vertical polarisation which uses horns as feed ports and coaxial probes as receive ports, and the parallel plate wave propagates in the TEM mode. The second uses horizontal polarisation which uses horns for both the feed and array ports, and the parallel plate wave propagates in the TE_1 mode. We investigated the former as it is a simpler technique. Both use feed ports which propagate in the fundamental TE mode, as opposed to the TEM mode of microstrip lenses.

The radiation characteristics of the horn as been simulated, it is seen that the

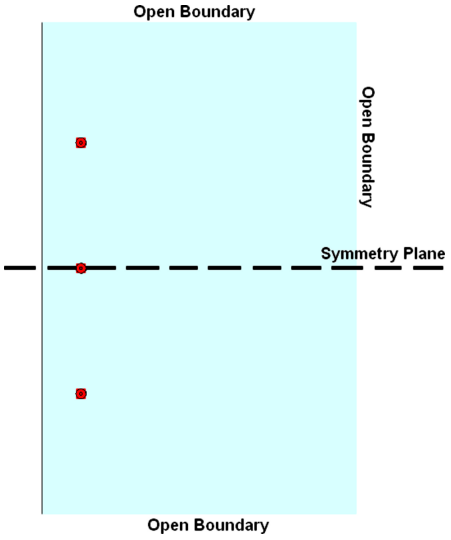

Figure 4.16: The CST model used to match an array port.

far-field phase of the radiated pattern deviates up to 4 degrees. The further the focal ratio departs from unity the more impractical it is to use equal sized ports on the beam contour. We summarised a method to customise the port dimensions to the contour.

The lens represents an electrically large space, where beam ports and array ports are within each others far-field. We can thus match them to the parallel plate separately. Two-variable parameter sweep are used to match the ports. The ports essentially follow periodically after each other, thus individual ports can be simulated using periodic boundries to reduce simulation time. A general design procedure to implement these lenses in waveguide for vertical polarisation is provided.

Chapter 5

Reflections Within the Lens

5.1 Introduction

In this chapter we design and simulate a traditional Rotman lens for a set of specifications. This Rotman lens is "traditional" in that it uses the α_2-β relationship given by Rotman and Turner in equation 3.34. A five-feed, eleven-element, Rotman lens with a maximum scan angle of 30° is designed for. The design process follows the procedures discussed in section 3.5 for the lens geometry and section 4.4 for the waveguide implementation, and serves as an example. Results from the simulation are then discussed.

The lens suffers from excess conjugate-port coupling, and it is shown by looking at the time domain signals that reflections off the array contour is the problem. By approximating the array contour as a reflecting wall, a mathematical model reveals focusing of the reflected energy onto conjugate ports. In the next chapter we design a lens for defocused reflections.

5.2 The design and simulation of a traditional Rotman Lens

5.2.1 The geometrical design and waveguide implementation

Table 5.1 shows the set of specifications chosen for the lens. Following the design procedure, we find that an appropriate value for the focal length is $Ł_1 = 7\lambda$ for a moderate angle ratio of $\gamma = 1.2$. This gives an array contour slightly bigger than the beam contour to reduce spillover losses, and array ports are spaced about 0.6λ apart. Sweeping the focal angle α_2 for least phase error, where β is given by equation 3.34 for a traditional Rotman lens, gives us the values: $\alpha_2 = 21.94°$ and $\beta = 0.9317$.

Table 5.1: Specifications of the lens.

Parameter	Symbol	Specification
Frequency	f	3.5Ghz
Beams	A	5
Array elements	B	11
Element spacing	d	0.5λ
Maximum scan angle	ψ_{max}	30°

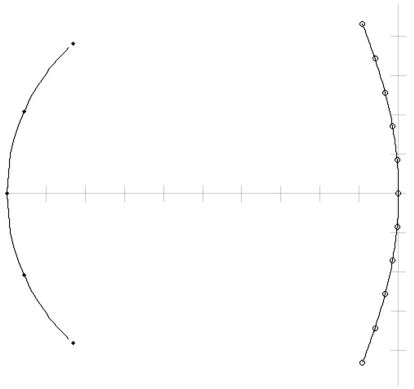

Figure 5.1: The lens geometry

The geometry for this lens is shown in figure 5.1. This value of γ gives the maximum inner-lens angle as $\theta_{max} = 24.62°$. The beam contour is left circular, thus $\rho = 1$. The value for ζ_{max} is 0.4286. The worst phase error is predicted to only be 0.08 degrees, practically negligible.

For traditional Rotman lenses the electrical delay difference in the transmission lines connecting array ports and elements is small. This delay between transmission lines implemented in coaxial cable is shown in millimeter units for the top array elements in table 5.2. The delay is relative to the on-axis array element.

Table 5.2: The relative phase difference in mm length between coaxial transmission lines used in the delay path.

Element Number	Delay (mm)
1	-2.23
2	-0.18
3	0.33
4	0.26
5	0.08
6	0.00

Following the design procedure given in section 4.4, figure 5.2 shows the waveguide cavity with the coaxial probe positions.

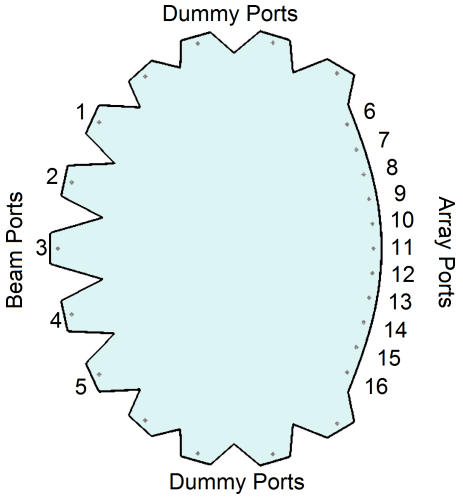

Figure 5.2: The waveguide cavity with beam and array ports numbered.

5.2.2 Simulation results

The structure shown in figure 5.2 was simulated in CST:MWS, with the ports optimised by the parameter sweeps as discussed in section 4.4. Figure 5.3 shows the reflection coefficient of beam port 2 when used in different CST models. It is first simulated and matched using the single port model shown in Figure 4.15. The problem is that this model ignores the influence from the rest of the lens structure and must therefore be validated. The port model is therefore simulated again but includes the rest of the beam ports on the beam contour. The sidewalls and array contour are left as an open boundary. Finally, the model is simulated again but the array ports are included in the structure. Figure 5.3 shows that the resulting match is still acceptable and validates the original model used to match the horn, saving simulation time. The matching of the array port follows from the same procedure. Simulations of an array port in various models is shown in figure 5.4.

As it is symmetrical about the horizontal axis, we only need to simulate excitations from ports 1, 2, and 3. The phase at the array elements is the resulting phase at the array ports with the port de-embedded by a distance shown in Table 5.2. The scanning operation of antenna arrays is dependent on a linear phase gradient across

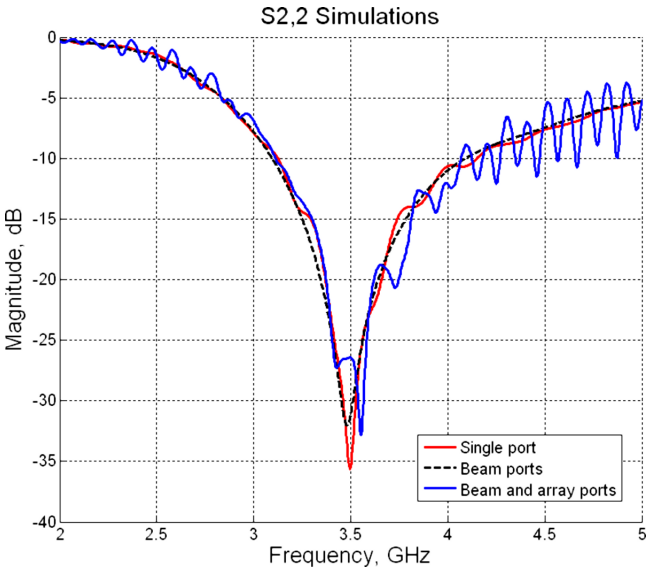

Figure 5.3: Port two's simulated reflection coefficient, with the inclusion of various structures.

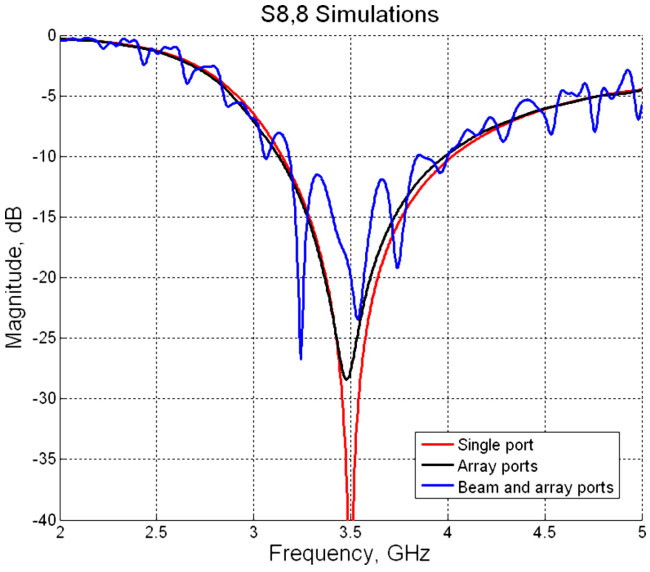

Figure 5.4: Simulated reflection coefficient of an array port, with the inclusion of various structures.

its elements. This gradient, in degrees, is given by

$$k = d \sin \psi \times 360^\circ \tag{5.1}$$

where d is the distance between elements in wavelengths, and ψ is the beam scan angle. Thus, elements spaced at half a wavelength and scanning at an angle of 30° requires a 90° linear phase gradient. If we compare this with the simulated phase gradient we get the phase error at each element.

With the gradients normalised to the on-axis element, Table 5.3 shows the simulated phase errors. According to the lens equations there should not be errors larger than a degree, thus there is a large disagreement between the prediction and the results. Although the beam port horns' phase centres are not perfect and each have shown phase errors up to 4 degrees, table 5.3 shows phase errors of up 56.3 degrees. In literature this is attributed to the reflections off the lens sidewalls[10], however, a simulation where the lens sides are perfect absorbers, or open boundaries, had little benefit compared to these results. The array beam is not very sensitive to small errors in amplitude and phase[16], but phase errors larger than about a tenth of a wavelength, 36°, begin to adversely affect the side lobe levels[7]. Table 5.3 further shows that the predicted phase errors for small lenses are negligible compared to those practically realised.

Table 5.3: Simulated phase errors, in degrees, at the array elements from the first three beam ports.

	Scan angle		
Array port	0°	±15°	±30°
6	8.3	-18.3	17.9
7	4.5	2.7	-3.5
8	-2.9	10	-12.2
9	5.1	-1.8	2.8
10	15.6	-8.5	2.7
11	0	0	0
12	17.8	-3.6	2.7
13	5.5	-0.02	2.8
14	21	5.9	-12.2
15	17.2	-11.2	-3.5
16	56.3	-26.7	17.9

The amplitude taper of the array ports is shown in figure 5.5. The on-axis port, port 3, shows coupling which is expected. However, the off-axis ports show couplings with larger errors. The reflection coefficients of the beam ports is shown in figure

5.6. We see that the on-axis port's S3,3 magnitude is approximately 6dB higher than the rest. It is found that this is a result of the reflections off the array ports. We discuss this further in the next section.

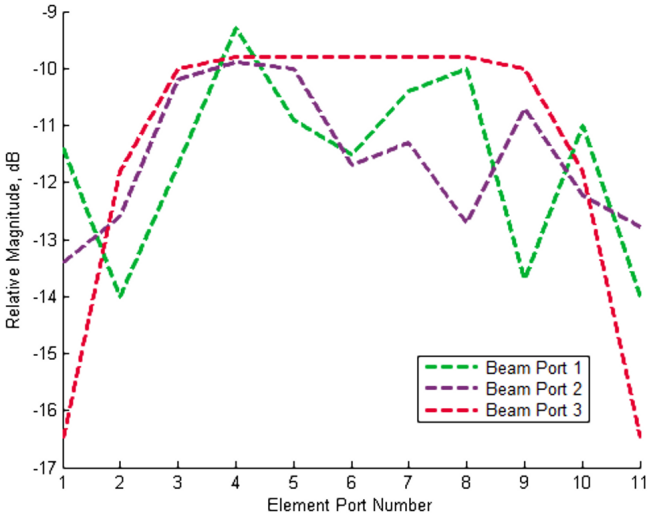

Figure 5.5: The amplitude taper of the antenna array, at 3.5GHz

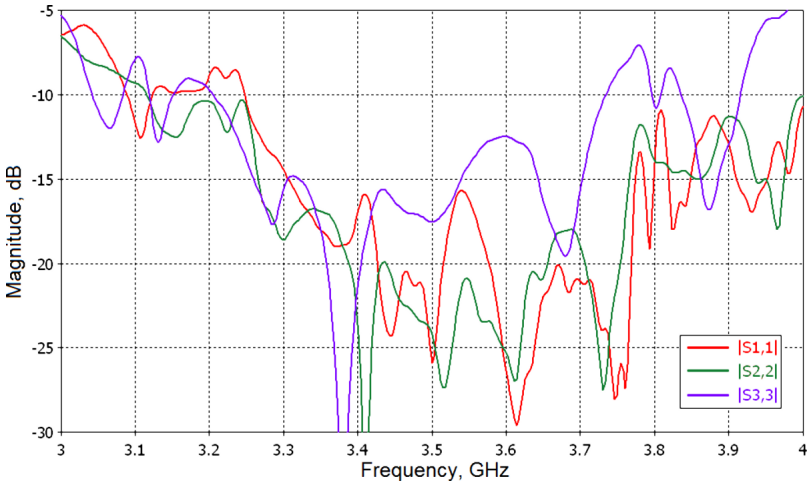

Figure 5.6: The reflection coefficients of beam ports 1 to 3.

5.3 The Conjugate-Port Coupling Problem

5.3.1 Defining the problem

When energy is coupled into the lens it radiates across the electrically large parallel plate region. Only a portion of the energy incident on a port gets absorbed, while the rest bounces back. This causes multiple reflections to exist within a lens giving rise to unwanted coupling between certain ports. The problem is quite severe in that it is the leading cause as to why some of these lenses fail to meet commercial specifications[10]. Some Rotman lenses have been known to have excess coupling between conjugate beam ports[2][11], exceeding the other beam port mutual couplings by up to 10dB. Smith states that "this is a focusing effect due to the geometry of the lens"[2]. Our lens has the same problem. For the beam ports' reflection coefficients we see that in figure 5.6 the on-axis port, port 3, doesn't achieve the same performance. This is not due to the mismatch between the port horn and the parallel plate region, but rather due to the mismatch at the array contour which is coupling back into port 3 as revealed in figure 5.7. Here we see two time signals of port 3, the emitted signal and the signal reflected back, and the signal received at the on-axis array port. The first reflection at about 0.8ns is the port mismatch, the second signal at about 5.5ns is the energy reflected off the array contour. We know this because the time between the input signal and the received signal at the array ($\pm 2.53ns$) is about equal to the time between the signal at the array and the second signal received at the beam port ($\pm 2.56ns$). Creating a mismatch at the array ports greatly increases the reflected signal.
As for the off-axis beam ports, the energy reflected off the array contour couples with the symmetrically opposed beam port. This is given by the time signal result shown in figure 5.8. Here the edge port's radiated signal is plotted with the reflection coefficient and the signal received by the conjugate port. We call this the conjugate-port coupling.

5.3.2 Modeling the reflections

Understanding or predicting the reflections off the array contour is the first step in finding possible solutions. We applied two models for the purpose of predicting these reflections. First we approximate the array contour as a reflecting wall. We can then assume the rays reflect off the wall at an angle described by Snell's law of reflection; the angle between the reflected ray and surface normal is equal to the angle between the incident ray and surface normal.

Figures 5.9 and 5.10 show rays traced (grey) from the on-axis and edge beam

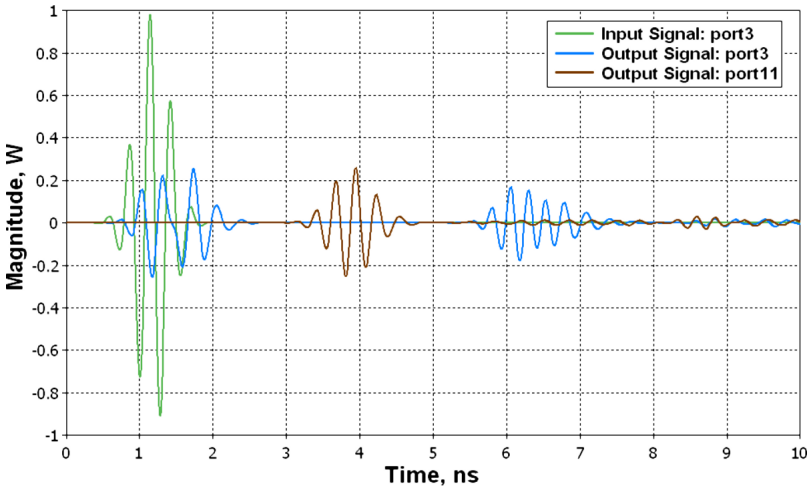

Figure 5.7: Simulation results showing the transmitted and received signals at the on-axis beam port, as well as the received signal at the on-axis array port.

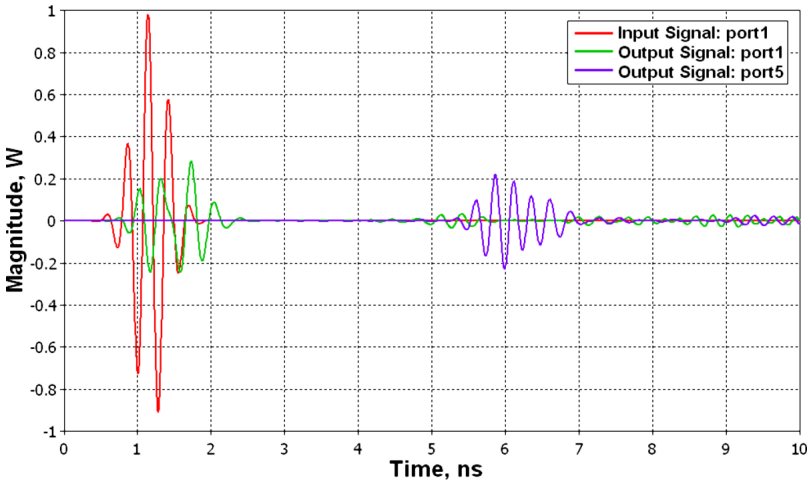

Figure 5.8: Simulation results showing the transmitted signal at the edge port and the received signal at the conjugate edge port.

ports respectively, to points on the array contour with their corresponding reflections (black). In figure 5.9 the reflections focus at a point just before the on-axis port. Figure 5.10 shows the reflections focus at a point just before the conjugate port. We can therefore deduce that this focusing of the reflected energy may be the cause of excess conjugate-port coupling. In the second model we make the simplification that a ray incident on the array contour reflects back equally in all directions across the parallel plate. For this model we simply find the distances from a beam port to points

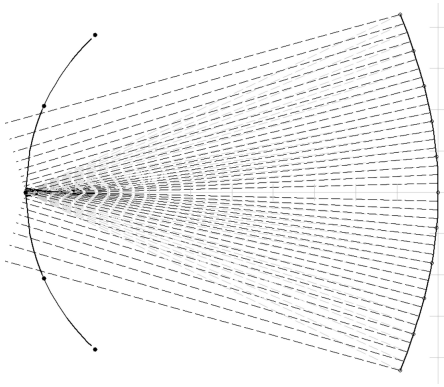

Figure 5.9: With the on-axis port as the source point, reflections plotted off the array contour focus just before the same port.

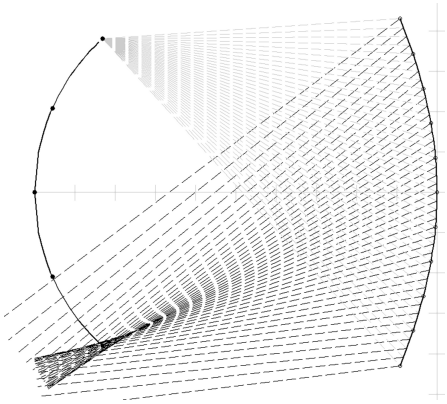

Figure 5.10: With the edge port as the source point, reflections plotted off the array contour focus just before the ports conjugate.

on the array contour and back to its conjugate. If we add up the rays over these distances we can predict if the reflections focus at the conjugate ports. The problem with these models is that they ignore the reflection and coupling coefficients of the ports. M. Maybell uses a ray structure method to model the coupling coefficients between ports of a microstrip Rotman lens[22].

We quantify the predictions of the two models by adding the complex information of the rays and then dividing by the total number of rays. Table 5.4 compares the two models to the simulation results for the edge and on-axis excitation ports. The first prediction is that of the Snell's law reflections off the array contour as shown in the above figures. Prediction 2 is the summation of path lengths taken from the source port to the array contour and back to the port of interest.

Table 5.4: Time domain signal amplitude received at a beam port from the reflection off the array contour for a given source port.

	Excitation Source: Port 1			Excitation Source: Port 3		
Port	Simulation	Pred. 1	Pred. 2	Simulation	Pred. 1	Pred. 2
1	0.0337	0	0.3245	0.0187	0	0.7937
2	0.0299	0	0.5673	0.0188	0.0789	0.9431
3	0.0187	0	0.7937	0.1690	0.6830	0.9998
4	0.0240	0.0690	0.9481	0.0188	0.0789	0.9431
5	0.2209	0.6633	0.9998	0.0187	0	0.7937

Because the coupling coefficients between ports are not incorporated, the models assume all the energy is reflected off the array contour and couples into a port. This is why the prediction values are much larger than the simulation's. However, the

models find their worth in that they may explain the cause of the excess conjugate coupling and give a reasonable indication to its severity. Figures 5.11 and 5.12 show the relationship between the predictions and simulation when all values are normalised to their maximum magnitudes. Prediction 1 reveals itself as a good precursor to excess conjugate-port coupling.

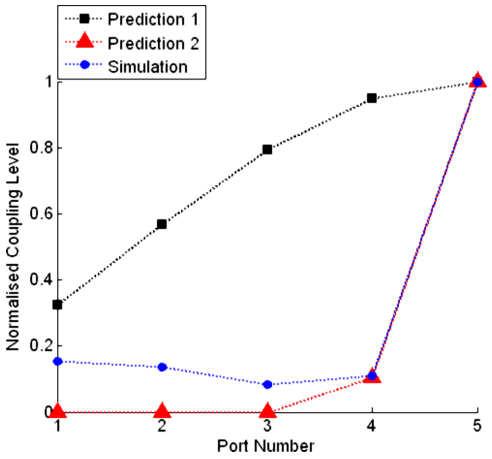

Figure 5.11: Comparison of the normalised beam port coupling from the reflections off the array contour. Port 1 is the source.

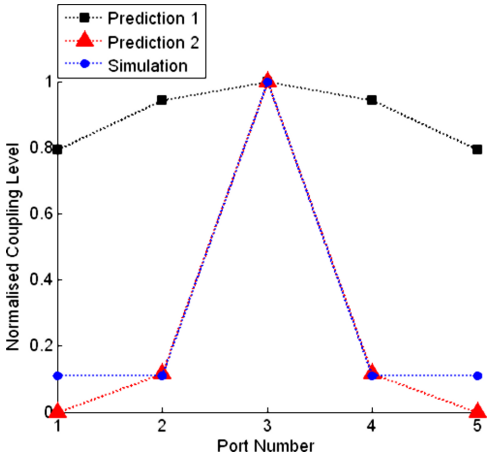

Figure 5.12: Comparison of the normalised beam port coupling from the reflections off the array contour. Port 3 is the source.

5.4 Conclusion

In this chapter we designed and simulated an example Rotman lens for a given set of specifications. The phase errors at the array ports larger than expected, a problem denoted to reflections off the lens sidewalls. Conjugate beam ports suffered from excess coupling, inhibiting the performance of the lens. Using the time domain results of the ports we are able to show that this coupling is due to the reflections off the array port.

A model which approximates the array contour as a reflecting wall was implemented, and shows the focusing of the reflected energy towards the conjugate port. As the model ignores reflection and transmission coefficients it cannot predict the actual conjugate-port coupling, however it does reveal the spread of the reflected energy between the beam ports. In the following chapter we investigate lens geometries which defocus the reflections from the conjugate ports.

Chapter 6

A Rotman Lens with Defocused Reflections

6.1 Introduction

In this chapter we design a Rotman lens for reflections defocused from the focal arc. The specifications of the lens are the same as the traditional Rotman lens designed in the previous chapter, this allows for comparison.

In section 5.3 we presented a model which shows the focusing of the reflected energy off the array contour. Here we analyse the effect of various array curvatures on these reflections. We show that Rotman lenses designed for minimum phase errors will have near maximum conjugate-port coupling. The design of a lens with reflections defocused from the beam ports comes at trade off with the phase errors, but we show that these phase errors are still negligible for most practical lenses.

Simulations of the new Rotman lens is presented and compared to the traditional Rotman lens. The defocusing was successfully shown, so we also constructed and measured the lens. For the most part, the measurements agree well with the simulated results.

6.2 Designing a Lens for Defocused Reflections.

6.2.1 Using the prediction model

In section 5.3 we defined a model to estimate the beam port to beam port coupling caused by reflections off the array ports, where the array contour was approximated as a reflection wall. This reveals focusing of the reflected energy as shown in figures 5.9 and 5.10. From the analysis of the lens parameters on the geometry, we know

that the edge focal angle, α, and the focal ratio, β, of the lens determines both the beam and array contour curvatures. Therefore, if any one of these parameters change so does the focus point of the reflections.

Modeling the reflections off the array contour of the traditional Rotman lens revealed that they focus just before the beam ports. This distance between the port and the reflection focus point is consistent for all conjugate-port reflections. It is seen that these reflections do not focus perfectly at a point, but rather in a small area. We can reasonably estimate the focus point, for the on-axis port, as the point where two symmetrical reflections taken from halfway up the array contour meet on the horizontal axis.

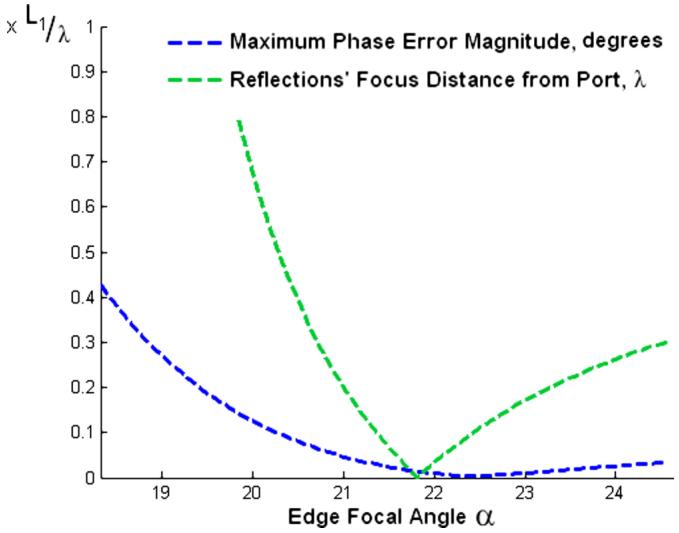

Figure 6.1: The phase error and the reflection's focus position as a function of α. Here $\beta = 0.9317$, corresponding to the traditional Rotman lens previously designed.

Using this method we can plot the distance between the port and the reflection's focus. A value of zero indicates that the reflections focus directly on the port and therefore the conjugate-port coupling will be at its maximum. Figure 6.1 shows this plot, along with the lens's maximum phase error, for different values of α. This plot is for a constant $\beta = 0.9317$, the same value used in the traditional Rotman lens previously designed. The reflection's focal point falls beyond the beam port for small values of α, and as α increases the focal point falls in front of the beam port.

The α used for the traditional Rotman lens was 22°, which will have reflections almost focused onto the conjugate ports according to the plot. Various lenses agree, the α-β relationship that results in the least phase errors across the aperture almost

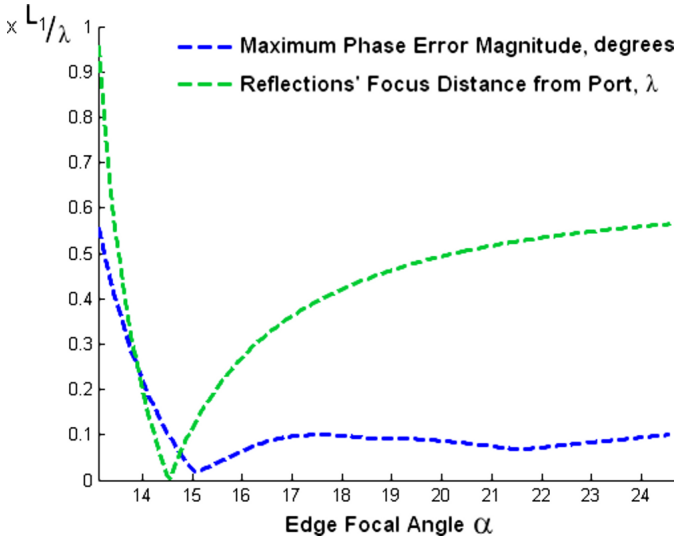

Figure 6.2: The phase error and the reflection's focus position as a function of α, for a focal ratio $\beta = 0.97$.

coincides with the point of maximum conjugate-port coupling. As β increases, these nulls move down the α axis, as shown in figure 6.2. Here β is chosen as 0.97. A traditional Rotman lens, where α and β are linked by equation 3.34, will use an α value of 14.25°, a lens that is likely to suffer from excess conjugate-port coupling. For a lens where the reflection's focal point falls further away from the conjugate port we may again choose an α of about 22°, for the β used in figure 6.2. At this point, the phase error is still below $0.1° \times L_1/\lambda$. Recall that the focal length, L_1, is the scale and width of the lens in wavelength. Thus, if phase errors below 10° were a prerequisite we could still have lenses up to 100 wavelengths in width, this incorporates most practical lenses[3]. However, the phase errors degrade with an increase in maximum scan angle. If $\psi_{max} = 50°$ the minimum normalised phase error achieved with defocused reflections is about 0.36°, allowing lenses up to about 30 wavelengths in width.

Table 6.1: The Rotman lens parameter values chosen for defocused reflections.

Parameter	Symbol	Value
Focal angle 1	α_1	$0°$
Focal angle 2	α_2	$22°$
Focal length ratio	β	0.97
Maximum scan angle	ψ_{max}	$30°$
Angle ratio	γ	1.2
Focal length	L_1	6λ
Array element spacing	d_e	0.5λ
Ellipse eccentricity	ρ	1

We will now design the geometry of a Rotman lens for the same set of specifications as the previously simulated lens. With α and β chosen as $22°$ and 0.97 respectively, we modify the remaining parameters so that the resulting lens will have beam and array contours of approximately equal height. The parameters are given in table 6.1. The array contour curvature is stronger compared to the previous Rotman lens, and the reflections plotted using the above mentioned model are shown in figures 6.3 and 6.4. The energy doesn't focus at a port, but is spread across the ports.

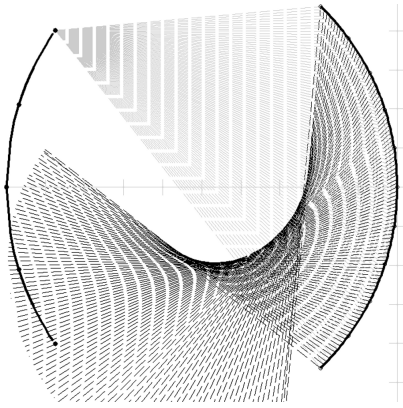

Figure 6.3: Reflections traced off the array contour from the edge port.

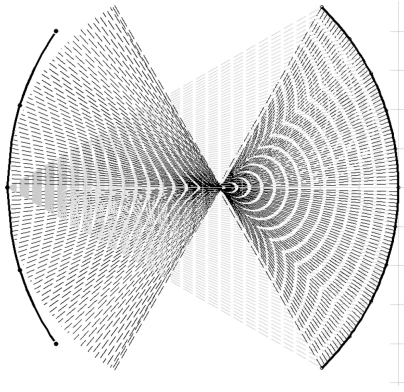

Figure 6.4: Reflections traced off the array contour from the on-axis port.

6.2.2 Waveguide implementation

The lens is implemented in waveguide, following the design procedure of section 4.4. Again, a centre frequency of 3.5GHz is used. The lens cavity along with the port numbers is shown in figure 6.5. This lens is a wavelength in width shorter than that

of the traditional Rotman lens, as the closed curvature of this array contour allows for a smaller lens to achieve the equal beam and array contour heights.

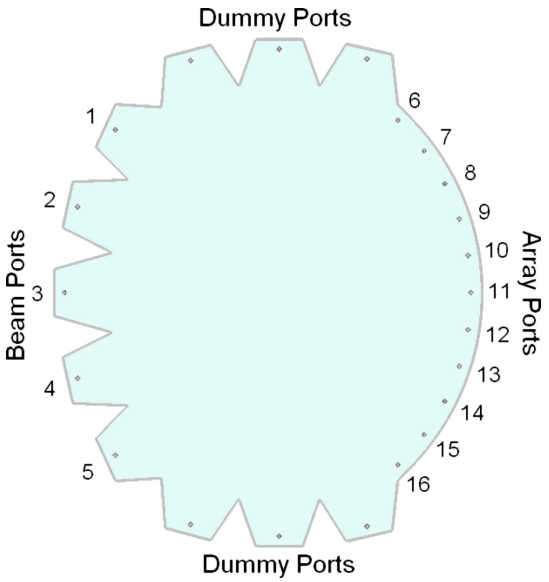

Figure 6.5: The lens's waveguide cavity with coaxial probe positions shown.

6.2.3 Simulation results

The lens was simulated in CST:MWS. The resulting phase errors at the elements are shown in table 6.2. For the most part, they are reasonable and compare well to that of the traditional Rotman lens. However, the 40° errors at elements 6 and 16 for the on-axis beam are unexpected.

The previously simulated Rotman lens suffered from excess conjugate-port coupling. Figures 6.6, 6.7 and 6.8 compare this lens, lens 1, with the lens 2, where the reflections are defocused from the beam contour. The conjugate-port coupling, specifically from port 1, caused lens 1 to achieve zero bandwidth at 15dB, whereas lens 2 achieves 8.5% bandwidth.

Figure 6.9 shows a comparison of the coupling levels between the two lenses, along with the predicted level. The simulated and predicted levels are separately normalised to the maximum level between them. Since the actual coupling levels are dependent on the port matching. The purpose of this figure is to show that the model predicted the spread of the reflected energy across the beam ports with a good degree of accuracy.

Table 6.2: Individual phase errors, in degrees, at the array elements from the first three beam ports. The element numbers coincide with the array element numbers shown in figure 6.5.

	Scan angle		
Array port	0°	±15°	±30°
6	-38.3	-29.5	-40
7	-12.7	-29.3	6.1
8	-9.9	18.7	4.3
9	-3.7	-11.0	9.5
10	-17.4	15.4	6
11	0	0	0
12	5.4	12.5	6
13	8.3	-4.3	9.5
14	6.4	9.4	4.3
15	8.5	15.6	6.1
16	-1.8	-6.3	-40

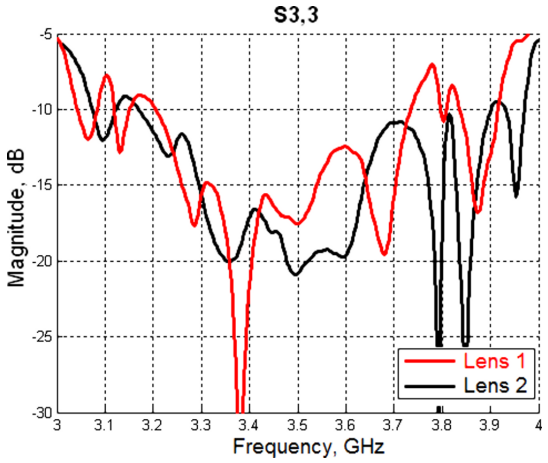

Figure 6.6: Comparison of the on-axis reflection coefficient for the traditional Rotman lens, lens1, and the lens with defocused reflections, lens2.

Since the performance of these lenses are based on reflections, the time domain transform of the simulations are informative. Figures 6.10 and 6.11 show the time domain S-parameters of the on-axis port reflections, S3,3, and the edge port conjugate coupling, S5,1. The reflections off the array contour is seen at about the 6ns mark. The time shift between the reflections for the two lenses is due to their different focal lengths, where the traditional Rotman lens is a wavelength, ±85mm, wider. This shows the reflection specifically off the array contour is reduced about 5dB for the lens with defocused reflections.

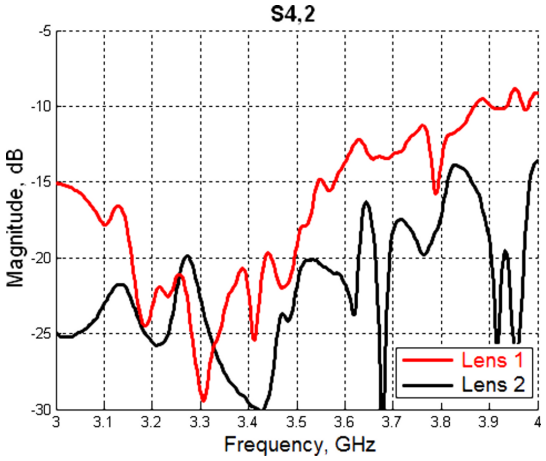

Figure 6.7: Comparison of the S4,2 conjugate-port coupling for the traditional Rotman lens, lens1, and the lens with defocused reflections, lens2.

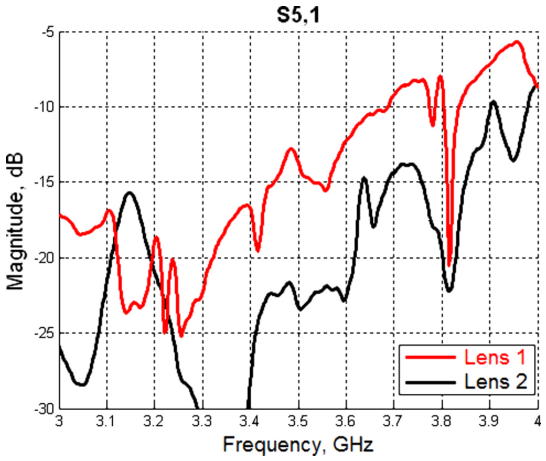

Figure 6.8: Comparison of the edge-port conjugate coupling for the traditional Rotman lens, lens1, and the lens with defocused reflections, lens2.

The minor reflections that is seen before and after the array contour reflection is primarily due to the sidewalls of the lens. Figure 6.12 compares the simulation of the lens with the sidewalls replaced by a perfect absorber. The reflection off the array contour remains constant as expected, but the minor reflections are reduced by about 20dB. The simulated radiation patterns of the two lenses are similar. Side-lobe levels range from about -17dB from the broadside beam to about -15dB for the edge beam.

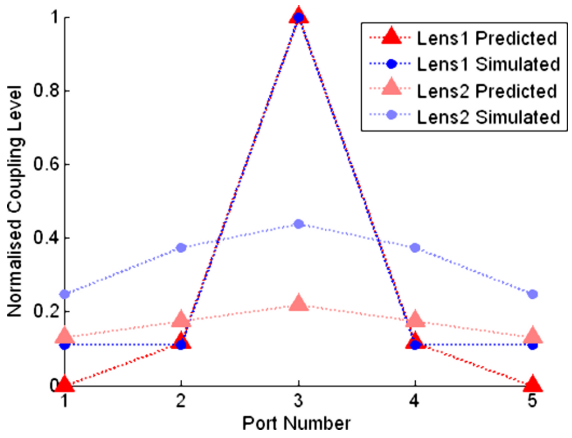

Figure 6.9: Comparison of the predicted and simulated normalised coupling levels for both lenses. The input is from port 3.

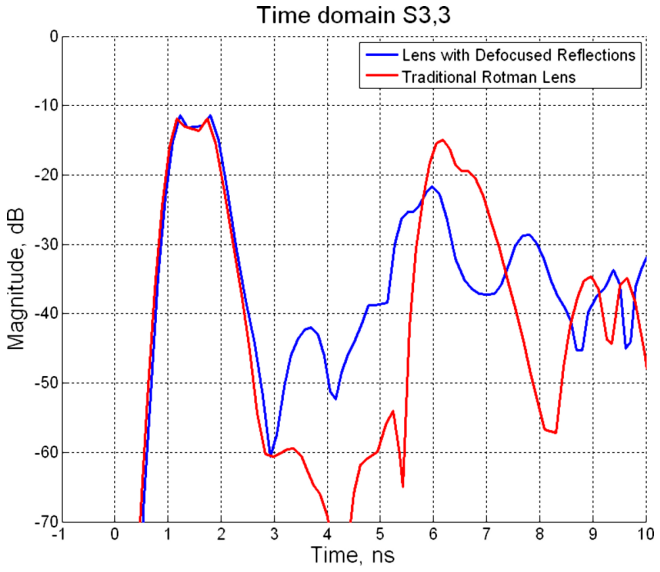

Figure 6.10: Comparison of the time domain transform of the simulated lenses, for the on-axis port.

6.3 Construction of the lens

The lens shape was laser cut out of aluminium sheets. As the laser struggles to cut thick plates, three 10mm plates were cut and stacked to make up the 30mm height requirement of the lens cavity. The lens was closed by using two sheets of 2.5mm thickness. SMA connectors are used for the ports. Their implementation in the lens is depicted in figure 6.13. The screws are countersunk from inside the lens and aluminium tape is applied over the screw to allow for a smooth conducting

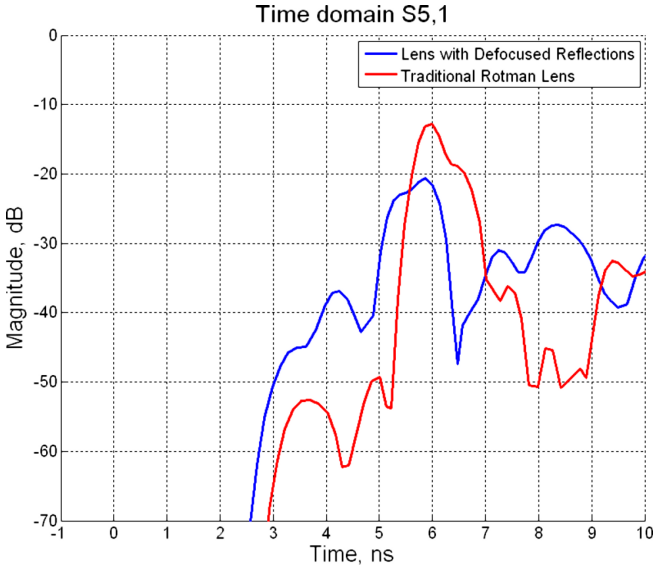

Figure 6.11: Comparison of the time domain transform of the simulated lenses, for the edge port.

surface. A conductor with a hole drilled in it on one side is soldered to the SMA's solder bucket, this is to probe the lens cavity with correct length for the impedance matching. The 2.5mm air gap between the SMA connector and the lens cavity is accommodated for in the simulations for the port matching.

The lens is quite cumbersome with dimensions of 670 x 780 x 35mm and weighing at about 18kg. The manufacturing tolerances of the aluminium cutting is about ±1mm, whereas the connector positioning is about ±0.5mm, and the coaxial probe lengths are about ±0.2mm.

6.4 Measurements

The measurements of the lens was done on a vector network analyser, where the S-parameters of the ports were taken two at a time while the other ports were connected to 50Ω matched loads. Figure 6.16 shows the reflection coefficients of the beam ports as well as the conjugate-port coupling. The bandwidth achieved is about 3% at -15dB and 13% at -10dB, compared to 8.5% and 18% achieved by the simulation. Recall that the traditional Rotman lens simulation achieved 0% and 12.6% bandwidth respectively. Although, in all cases, these values may sightly improve if more time is spent tuning the port matching.

Figures 6.17 through 6.21 show plots comparing the reflection coefficients and conjugate-port coupling of the three results. Lens1 is the traditional Rotman lens

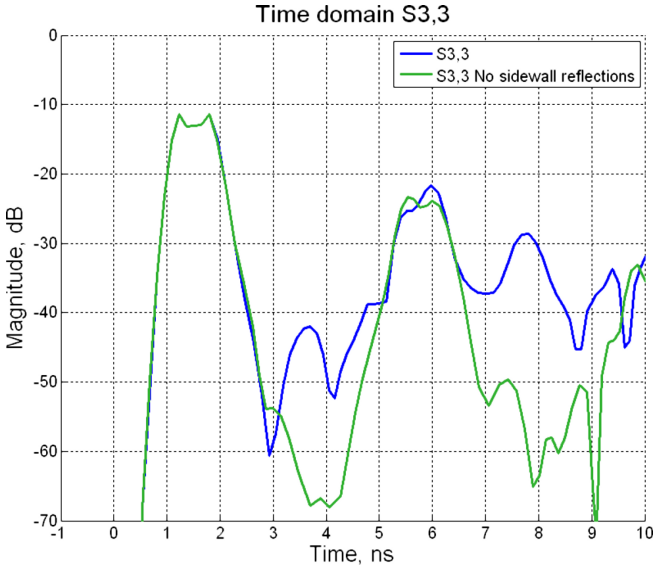

Figure 6.12: Comparing the time domain transform of the lens with and without reflections from the sidewalls.

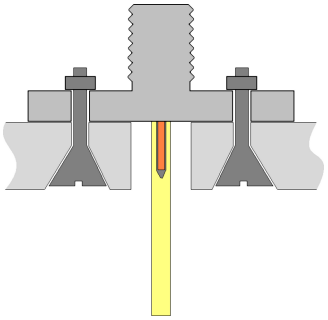

Figure 6.13: A side view of the SMA connectors used on the lens.

and Lens2 is the Rotman lens designed in this chapter for defocused conjugate-port coupling. The measured reflection coefficients of the off-axis ports are up to 5dB higher than that of the simulations. Applying the tolerances to the simulation show that they are likely the cause. Furthermore, the coupling between conjugate ports are between 5 and 8dB less than that of the simulations. Currently this is unclear why. Simulating the lens with aluminium instead of a lossless metal shows about 2dB less coupling. There happens to be a 1 to 3dB improvement in the measured array port matches. However, the measurements agree that the reflected energy off the array contour is spread across the lens, unlike the traditional lens where this energy is focused onto the conjugate-port. The maximum magnitudes of the

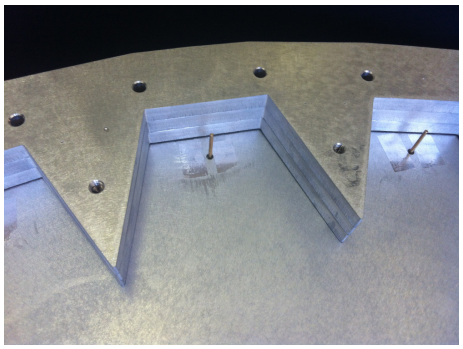

Figure 6.14: A photo taken of a beam port from inside the lens.

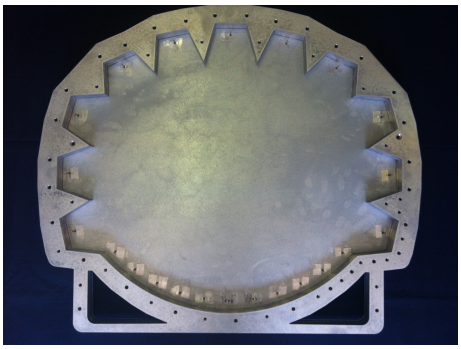

Figure 6.15: A photo of the lens constructed in waveguide, with the top plate removed.

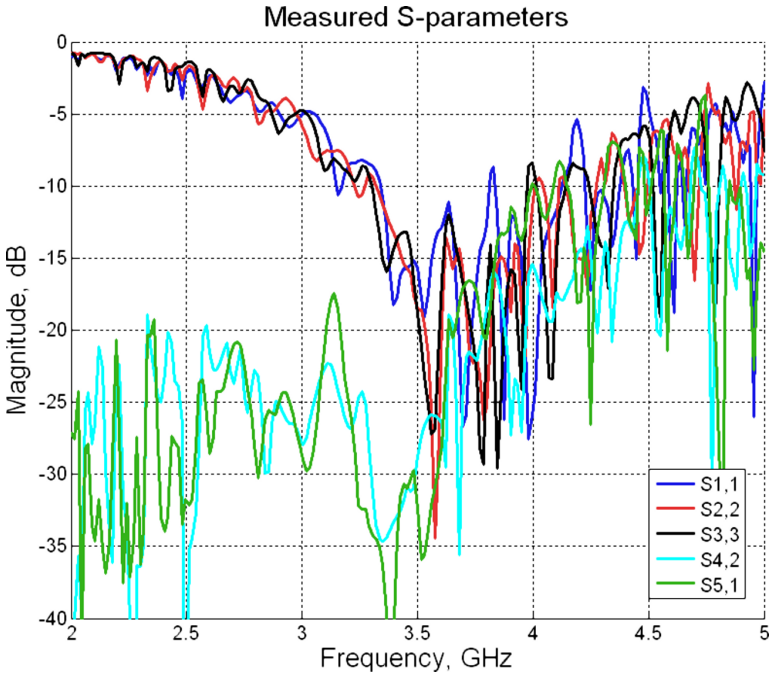

Figure 6.16: The measured reflection coefficients and conjugate-port coupling.

reflected energy measured and simulated at each port is shown in figure 6.24. These values are taken from the time domain transform between the 2 and 5GHz band, and reveal the energy spread across the beam contour.

The phase errors of the measured results are shown in table 6.3. They compare well to the simulated phase errors of table 6.2. The coaxial line phase delay between the array ports and elements were not included in the construction, therefore the

phase delay was manually added to the measured phases at the array ports.

E-plane horns were simulated for use on the antenna array, which produces the radiation pattern shown in figure 6.25 for the measured amplitude and phase tapers. The beams fall within about 1.5 degrees of their required direction, and have half-power beamwidths of about 11°. The beams cross over at about -7dB. Methods to increase the cross-over level include the addition of more beam ports, a lower scan angle, or designing for a different array element spacing. The side-lobe levels are about -16.5dB for the broadside beam to about -13dB for the outer beams.

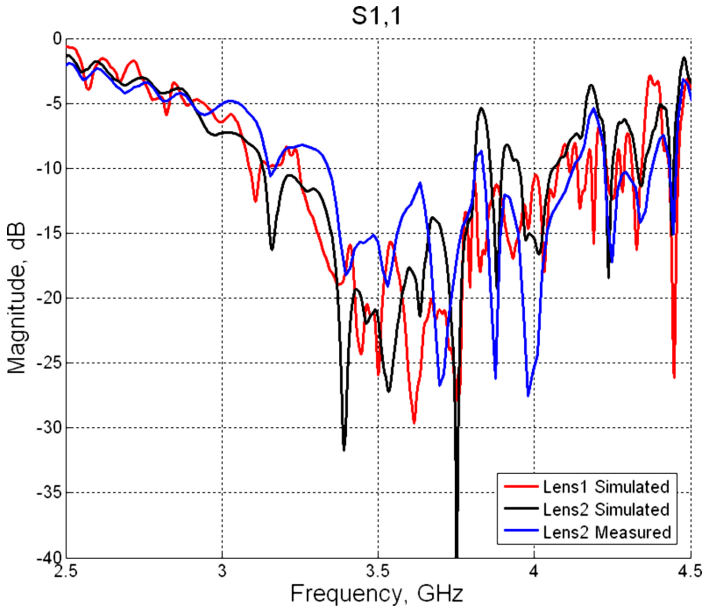

Figure 6.17: Comparison of the reflection coefficients for port 1.

6.5 Conclusion

In this chapter we designed, simulated, and constructed a Rotman lens in waveguide which shows reduced conjugate-port coupling compared to that of the traditional Rotman lens which was designed and simulated in the previous chapter. We have shown that any trifocal lens designed for minimum phase errors will have its reflected energy focused at a conjugate port. Defocusing the reflected energy was accomplished by closing the curvature of the array contour, this is done by increasing both the focal ratio and the edge focal angle.

Measurements agree with the prediction model of the previous chapter that the reflections off the array contour are spread across the beam ports, as opposed to the

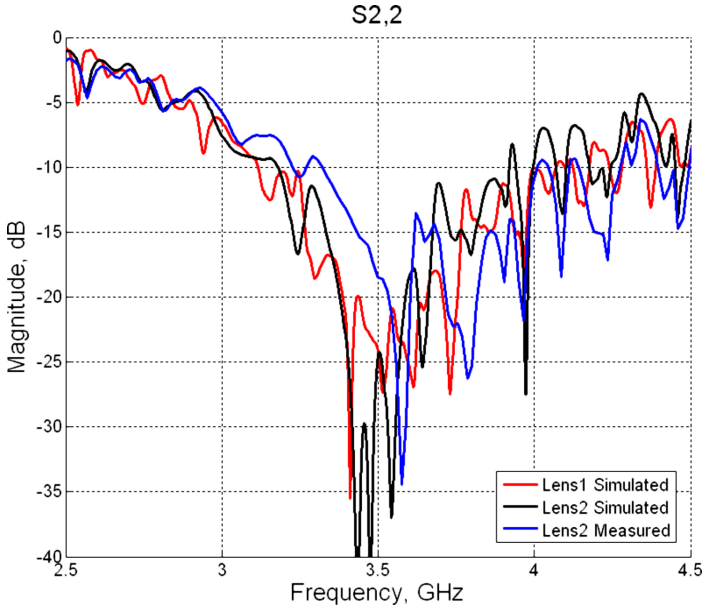

Figure 6.18: Comparison of the reflection coefficients for port 2.

Table 6.3: Individual phase errors, in degrees, taken from the phase measurements at the array elements for a given source port.

	Scan angle		
Element	0°	±15°	±30°
6	-27.4	-20.6	-39
7	-4.3	-29.3	1.8
8	-0.8	24.3	1.3
9	1.7	-4.2	8.9
10	-16.3	14.9	3.3
11	0	0	0
12	10.2	12.8	1.1
13	12.4	2.6	8.2
14	10.2	17.1	1
15	7.8	15.5	1.7
16	3.4	-7.3	-43.4

focusing of the reflections toward a single beam port.

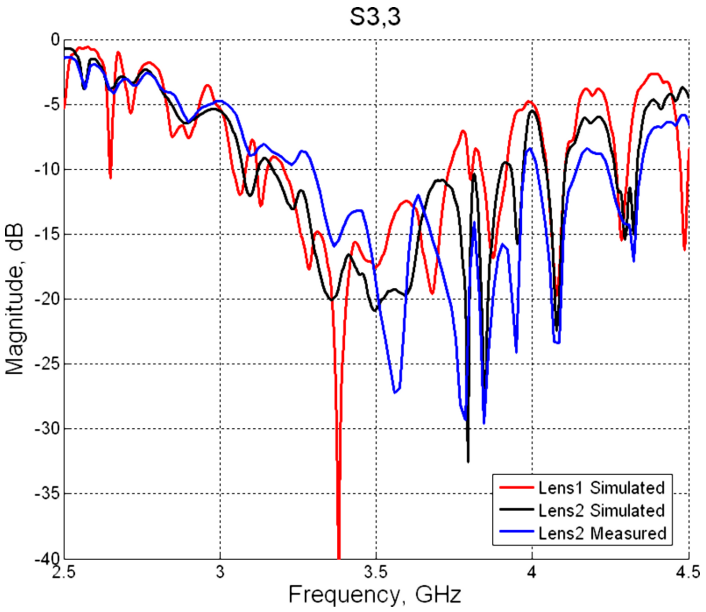

Figure 6.19: Comparison of the reflection coefficients for the on-axis port.

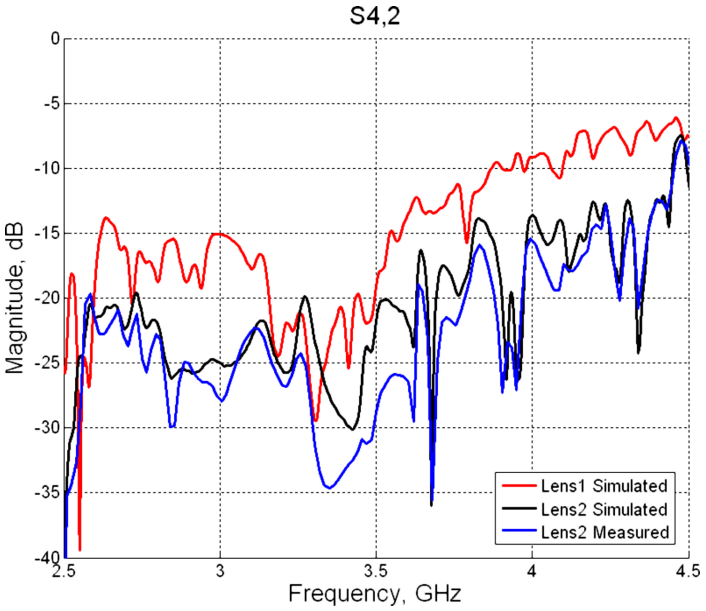

Figure 6.20: Comparison of the conjugate-port couplings of port 2 and 4.

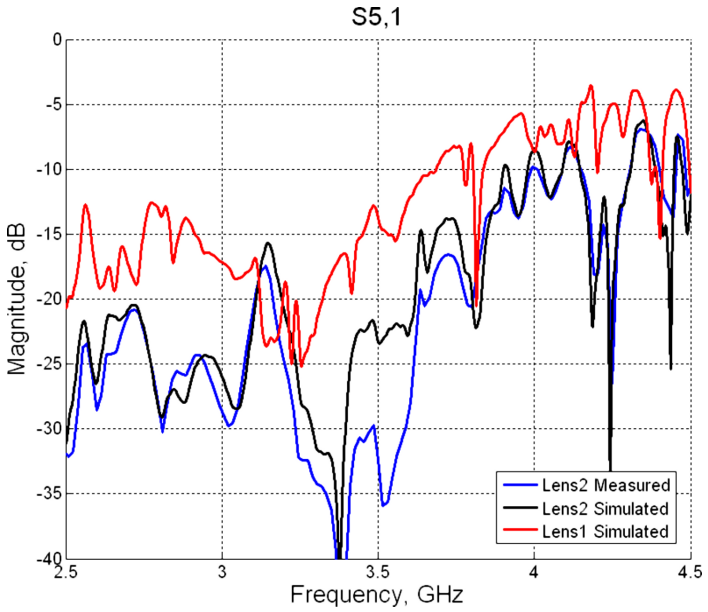

Figure 6.21: Comparison of the conjugate-port couplings of the edge ports.

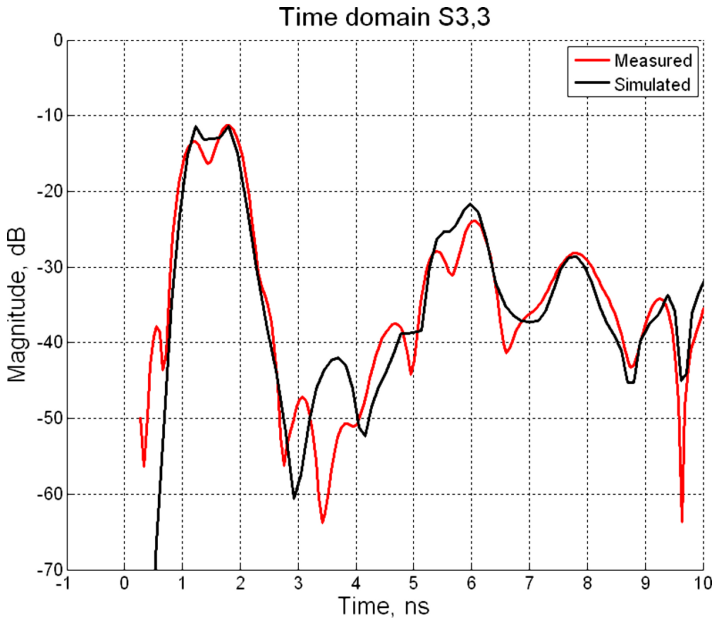

Figure 6.22: Time domain plot of the on-axis port's reflection.

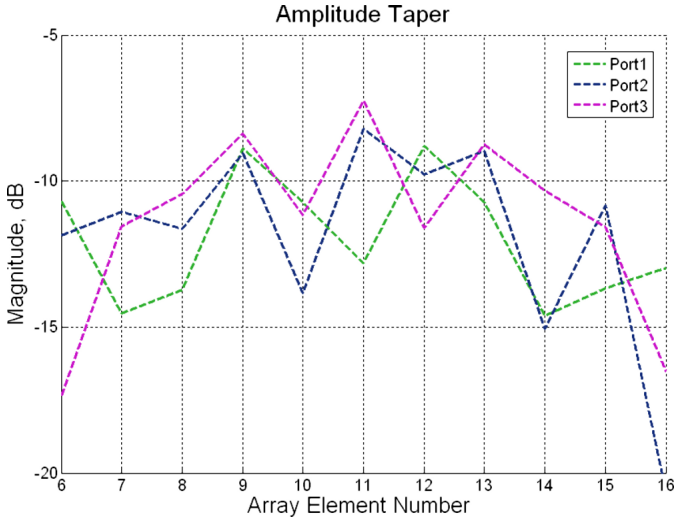

Figure 6.23: The amplitude taper at the array for a given source port.

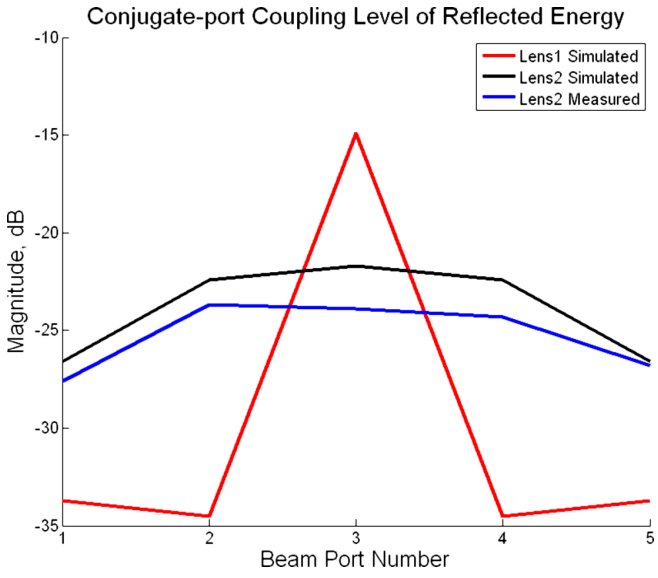

Figure 6.24: The maximum conjugate-coupling level of the reflected energy taken from the time domain.

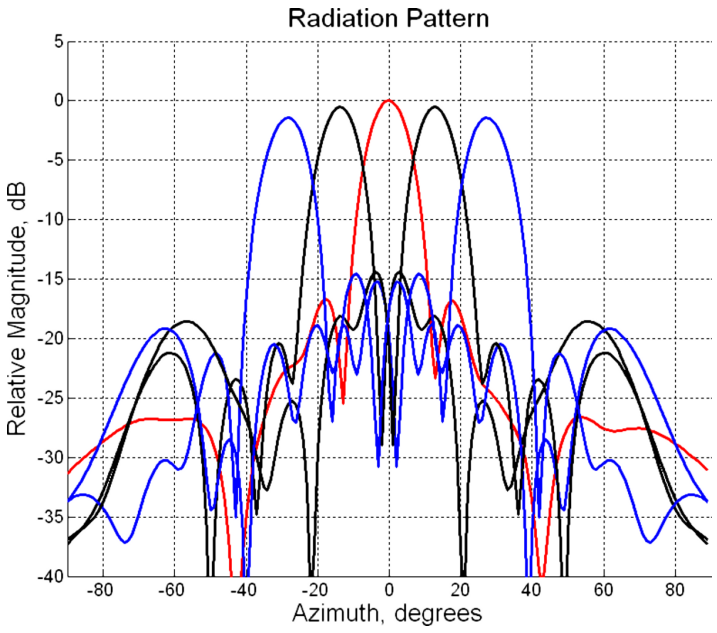

Figure 6.25: Simulated radiation pattern using measured amplitude and phase tapers.

Chapter 7

Conclusion

The Rotman lens has become synonymously known as a trifocal Bootlace lens. Although the lens equations provided by Rotman and Turner include a relationship between the focal ratio and focal angle which gives near minimum phase errors, not all Rotman lenses designed make use of it[16]. Those which do, we label traditional Rotman lenses. A degree of optimisation is required to reduce phase errors, however, slight deviations from the optimal phase errors still give a negligible degradation in performance for most practical lenses. We have shown that, for trifocal lenses, a deviation from the parameters which provide optimum phase errors is necessary to reduce conjugate-port coupling on the focal arc. Using the specifications listed in table 7.1 we designed two lenses, a traditional Rotman lens, and a lens which reduces the conjugate-port coupling.

Table 7.1: Design specifications for the Roman lenses.

Parameter	Symbol	Specification
Frequency	f	3.5Ghz
Beams	A	5
Array elements	B	11
Element spacing	d	0.5λ
Maximum scan angle	ψ_{max}	30°

The traditional Rotman lens used a focal ratio of $\beta = 0.93$ and a focal angle $\alpha_2 = 22^\circ$. The improved lens used a focal ratio of $\beta = 0.97$ for the same focal angle. Figure 7.1 shows the geometries of the two lenses. Excess conjugate-port coupling was predicted by modeling the the array contour as a reflecting wall. Due to the coupling coefficients being ignored, exact levels of coupling cannot be predicted. However, the model revealed focusing of the reflected energy for a Rotman lens with minimum phase errors. Closing the array contour curvature is the solution implemented here.

Simulations show up to 10dB reduced conjugate-port coupling between the lenses. Measurements of the lens show less conjugate-port coupling, but strongly agree with the spread of the reflected energy across the focal arc. The reflected energy in a traditional Rotman lens focuses just before the conjugate port. Therefore, if the lens is large with many beam ports the reflected energy may spread over a few ports rather than only coupling into one. This is convenient since large lenses will likely require optimised phase errors. For the Rotman lens we implemented in waveguide, a deviation from the optimal phase errors by using a stronger array contour curvature has reduced the conjugate-port coupling for a negligible degradation in scanning performance.

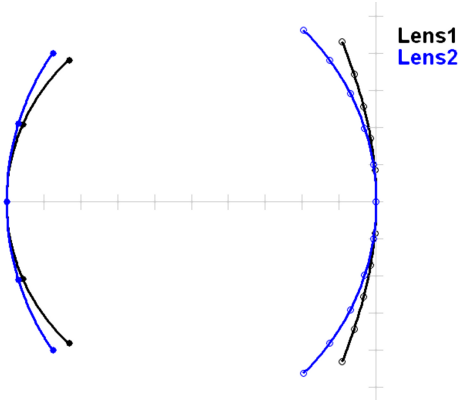

Figure 7.1: The geometrical change which defocused the reflections in the lens.

Quadrifocal lenses have their focal ratio restricted to $\beta = 1$. They should be used if equal sized horns are required for the beam ports. Although their phase errors are larger than that of a trifocal lens for $\beta \neq 1$, the reflections in quadrifocal lens are defocused from the focal arc. Due to the strong curvature of the quadrifocal lens it is restricted to a maximum scan angle of about 45°.

The defocused lens built and compared to simulations. Future work includes the manufacturing of the traditional Rotman lens as well, to allow for direct comparisons. The microstrip implementation of the Rotman lens is popular as the construction will be smaller and have broader bandwidth. We would therefore like to build and compare the a lenses in microstrip aswell. Due to the dielectric, losses in the microstrip lens will reduce coupling from the energy reflected off the array contour[23]. The dielectric constant needs to be included in the lens design equations[24], and the horns for all ports need to have their phase centres correctly positioned[20].

Bibliography

[1] D. H. Archer, "Lens-fed multiple beam arrays," *Microwave J.*, vol. 18, pp. 37–42, October 1975.

[2] M. S. Smith and A. K. S. Fong, "Amplitude performance of ruze and rotman lenses," *Radio and Electronic Engineer*, vol. 53, no. 9, pp. 329–336, September 1983.

[3] D. H. Archer, "Lens-fed multiple beam arrays," *Microwave J.*, vol. 27, pp. 171–195, September 1984.

[4] A. I. Zaghloul, O. Kilic, S. J. Weiss, and E. D. Adler, "Realization of rotman's concepts of beamformer lenses and artificial dielectric materials," *IEEE Trans. Antennas Propagat.*, pp. 1–4, November 2009.

[5] E. O. Rausch, A. F. Peterson, and W. Wiebach, "Millimeter wave rotman lens," *Proceedings of the 1997 IEEE National Radar Conference.*, pp. 78–81, May 1997.

[6] C. A. Balanis, *Antenna Theory Analysis and Design.* John-Wiley and Sons, Inc, 2005.

[7] R. C. Hansen, *Phased Array Antennas.* John-Wiley and Sons, Inc, 2010.

[8] W. Rotman and R. F. Turner, "Wide-angle microwave lens for line source application," *IEEE Trans. Antennas Propagat.*, vol. AP-11, pp. 623–632, November 1963.

[9] J. Ruze, "Wide-angle metal-plate optics," *Proc. I.R.E*, vol. 38, pp. 53–58, January 1950.

[10] L. T. Hall, H. J. Hansen, and D. Abbott, "2d scanning rotman lens structure for smart collision avoidance sensors," *Proceedings of SPIE - The International Society for Optical Engineering*, vol. 5274, pp. 93–99, 2004.

[11] K. Tekkouk, M. Ettorre, R. Sauleau, and M. Casaletti, "Folded rotman lens multibeam antenna in siw technology at 24 ghz," *Antennas and Propagation (EUCAP), 2012 6th European Conference on*, pp. 2308–2310, March 2012.

[12] J. A. Kong, *Electromagnetic wave theory.* John-Wiley and Sons, Inc, 1986.

[13] W. E. Kock, "Metal-lens antennas," *Proc. I.R.E*, vol. 34, pp. 828–836, November 1946.

[14] M. L. Kales and R. M. Brown, "Design considerations for two-dimensional symmetric bootlace lenses," *IEEE Trans. Antennas Propagat.*, vol. AP-13, pp. 521–528, July 1965.

[15] J. B. L. Rao, "Multifocal three-dimensional bootlace lenses," *IEEE Trans. Antennas Propagat.*, vol. AP-30, November 1982.

[16] R. C. Hansen, "Design trades for rotman lenses," *IEEE Trans. Antennas Propagat.*, vol. 39, pp. 464–472, April 1991.

[17] J. P. Shelton, "Focusing characteristics of symmetrically configured bootlace lenses," *IEEE Trans. Antennas Propagat.*, vol. AP-26, July 1978.

[18] D. M. Pozar, *Microwave Engineering.* John-Wiley and Sons, Inc, 2005.

[19] A. F. Peterson and E. O. Rausch, "Scattering matrix integral equation analysis for the design of a waveguide rotman lens," *IEEE Trans. Antennas Propagat.*, vol. 47, May 1999.

[20] J. L. Cruz, B. Gimeno, E. A. Navarro, and V. Such, "The phase center position of a microstrip horn radiating in an infinite parallel-plate waveguide," *IEEE Trans. Antennas Propagat.*, vol. 42, August 1994.

[21] E. O. Rausch and A. F. Peterson, "Rotman lens design issues," *Antennas and propagation society international symposium, 2005 IEEE*, 2005.

[22] M. Maybell, "Ray structure method for coupling coefficient analysis of the two dimensional rotman lens," *Antennas and Propagation Society International Symposium*, vol. 19, pp. 144–147, June 1981.

[23] A. K. S. Fong and M. S. Smith, "A microstrip multiple beam forming lens," *Radio and Electronic Engineer*, vol. 54, pp. 318–320, July 1984.

[24] D. R. Gagnon, "Procedure for correct refocusing of the rotman lens according to snell's law," *IEEE Trans. Antennas Propagat.*, vol. 37, March 1989.